



# An in-situ Raman study on the oxidation of mackinawite as a corrosion product layer formed on mild steel in marginally sour environments

Wei Zhang<sup>1,\*</sup>, David Young, Bruce Brown, Cody Shafer, Fei Lu<sup>2</sup>, Ezechukwu Anyanwu<sup>3</sup>, Marc Singer

Institute for Corrosion and Multiphase Technology, Ohio University, 342 West State Street, Athens, OH, 45701, USA

## ARTICLE INFO

### Keywords:

- A. Mild steel
- B. Raman spectroscopy
- B. XPS
- C. Acid corrosion
- C. Oxidation
- C. Pitting corrosion

## ABSTRACT

An *in situ* Raman flow loop with flow cell was developed to enable observation of the mackinawite corrosion product layer generated in marginally sour environments with traces of oxygen ingress. As a result, the mackinawite corrosion product layer was found to be oxidized into magnetite in the solution when  $[O_2]_{(aq)} > 3 \text{ ppb}_{(w)}$ , which was linked to the pitting initiation of mild steel (API X65) in marginally sour environments. The 2D precursor of nano-crystal mackinawite, the chemisorption FeS layer,  $S_{ads}(\text{Fe})$ , was detected by *ex situ* Raman microscopy.

## 1. Introduction

Understanding the structure and properties of surface layers is of key importance in the study of localized corrosion. Understanding mechanisms associated with the localized corrosion of steel in oxygen containing aqueous solutions has been the topic of a vast body of literature over the past century [1–4]. As stated by H. Strehblow: “One of the most important developments over the past 20 years in the study of passivity has been the application of surface analytical techniques” [5]. Mechanisms of localized corrosion of steel in carbon dioxide containing aqueous solutions have also received a lot of attention [6]. However, research on localized corrosion of mild steel in hydrogen sulfide containing solutions is relatively sparse due to the complexity of the required experimental methods due to the toxicity of  $H_2S$ . Therefore, a lot of work remains to be done on understanding the role of corrosion product layers formed in sour environments relating to localized corrosion.

In  $O_2$  containing aqueous solution, the layer growth begins after the adsorption of  $O_2$  on the steel surface. Usually, the thickness of the oxide layer is less than 100 nm. If these oxides films have semiconducting properties, as for the oxides of Fe, Cr, Ni, and Cu, they will grow only up to a few nanometers in thickness [7]. For example, the thickness of the passive film on stainless steel is usually up to only 5 nm [8]. The study of

this type of nano-scale films carries a lot of analytical challenges as very specialized techniques must be used. X-ray photoelectron spectroscopy (XPS) [9], secondary ion mass spectrometer (SIMS), extended X-ray absorption fine structure (EXAFS), Auger electron spectroscopy (AES) [10] and scanning tunneling microscope (STM) [11] are typically needed to identify passive layers and study their structures. Oxide layers are also often examined in cross-section analysis using transmission electron microscopy (TEM) enabling direct visualization of the layer.

It has been noted that the as-characterized passive layer structure could be different following *ex situ* and *in situ* materials analysis processes. This is because post-processing of the specimen (drying process, exposure to air) can lead to structural changes to the layers. For example, Bockris and co-workers [11] reported, using a transfer device for Auger analysis, that the passive film on iron is composed of  $Fe(OH)_2$ , forming a polymeric layered structure. O’Grady [12] used *in situ* Mössbauer spectroscopy to examine both *in situ* and “dried” (*i.e.*, *ex situ*) passive films. The *in situ* films consisted of chains of iron atoms connected by dioxy and dihydroxy bonds, further linked by water. However, the film changed to more closely resemble  $\gamma\text{-Fe}_2O_3$  upon removal from the passivating medium and upon drying and aging.

In  $CO_2$  environments, a  $FeCO_3$  precipitation layer can typically reach several tens of microns in thickness, plus incorporate residual  $Fe_3C$  inside. These layers are easily visible in cross section analysis under SEM.

\* Corresponding author.

E-mail address: [wz521414@ohio.edu](mailto:wz521414@ohio.edu) (W. Zhang).

<sup>1</sup> 7669 State Route 56, Athens, OH, 45701, USA. Current affiliation: Schlumberger, 6350 West Sam Houston Pkwy N, Houston, TX 77041.

<sup>2</sup> Current affiliation: National Energy Technology Laboratory, 626 Cochran Mill Road P.O. Box 10940, Pittsburgh, PA 15236-0940.

<sup>3</sup> Current affiliation: Exponent, Inc., 149 Commonwealth Drive, Menlo Park, CA 94025.

However, their degree of protectiveness has been linked to the presence and characteristics of a thin layer of oxide formed on the metal surface, rather than being ascribed to the presence of a thicker  $\text{FeCO}_3$  layer. FIB-TEM analysis was required to make this observation [13].

In sour environments ( $\text{H}_2\text{S}/\text{CO}_2$ ), study of the structure and properties of corrosion product layers is much more complicated because of the potential for numerous FeS polymorphs to co-exist as well as because of the complications associated with sulfur chemistry. A large body of knowledge does exist, derived from geochemistry research, particularly that related to the formation of mackinawite (FeS)/troilite (FeS)/pyrrhotite ( $\text{Fe}_{1-x}\text{S}$ ) as well as the  $\text{S}_2^{2-}$  containing mineral pyrite ( $\text{FeS}_2$ ). Pyrite typically forms at high  $\text{H}_2\text{S}$  pressure and high temperature [14]. Its conductivity has been used to explain the occurrence of localized corrosion and galvanic coupling between pyrite and steel [15]. Pyrite is the thermodynamically most stable product of several formation and transformation reactions involving mackinawite, greigite, troilite, and pyrrhotite [14]. On the other hand, mackinawite is often found to be the initial (kinetically favored) iron sulfide corrosion product forming on the substrate surface under most conditions [16]. Localized corrosion was also found at low  $\text{H}_2\text{S}$  partial pressure and low temperature [17–20]. Therefore, studies considering mackinawite, instead of pyrite, are crucial in understanding localized corrosion mechanisms in low temperature and low  $\text{H}_2\text{S}$  partial pressure environments. However, this is quite challenging because of the following aspects:

- 1) Mackinawite is unstable and easily oxidized during post-processing.
- 2) Freshly formed mackinawite is usually amorphous or nanocrystalline [21], which can lead to misidentification using typical diffraction-based techniques.
- 3) Mackinawite formed as corrosion product layer can be very thin at low temperature and low  $\text{H}_2\text{S}$  partial pressure, which can add to the difficulty of the analysis, especially when the substrate is actively corroding underneath.
- 4) The precursor or first few layers of mackinawite, which is formed by chemisorption ( $\text{S}_{\text{ads}}(\text{Fe})$ , [22]) is very difficult to detect using common analysis techniques.
- 5) The co-existence of other corrosion products or residual phases, such as iron oxides, iron carbide, and iron carbonate all increase the complexity of the analysis.

Therefore, it is necessary to find a suitable, preferably *in situ*, analytical tool to facilitate the study of localized corrosion in sour environments, especially when  $\text{H}_2\text{S}$  content is small (e.g., in marginally sour environments [17]).

Oxidation of mackinawite in the air at room temperature can readily occur, although it is logically not as fast as at higher temperature. Studies have reported only partial oxidation of mackinawite into another phase [16]. Therefore, if the layers of interest are thick enough (for example, if they are formed at comparatively higher  $\text{H}_2\text{S}$  partial pressure), scanning electron microscopy/energy dispersive X-Ray spectroscopy (SEM/EDS) and X-ray powder diffraction (XRD) can give satisfactory results and provide the correct phase identification information. XPS only provides information about the top several layers of atoms, consequently, XPS spectrum can provide information about surface oxidation of mackinawite. Cross-sectional analysis using the focused ion beam technique combined with transmission electron microscopy (FIB-TEM) could offer information about the entire layer. If further combined with selected area electron diffraction (SAED) and process electron diffraction (PED), phase identification is enabled, provided that the layer thickness is greater than 100 nm [18,19]. However, if the outer layer of mackinawite has been oxidized, no *ex situ* analysis could determine if the oxidation occurred due to the experimental environment or due to post processing. Therefore, *in situ* Raman spectroscopy is an appealing technique since:

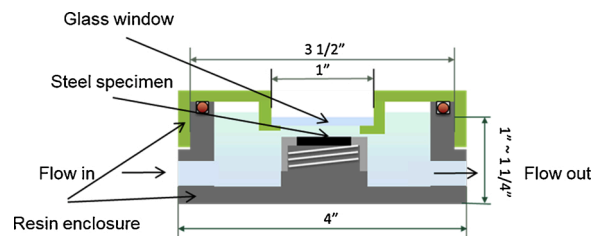


Fig. 1. 2D design sketch of the 3D printed *in situ* Raman flow cell (IRFC) reactor.

- 1) Raman spectroscopy is relatively simple to use and does not require vacuum.
- 2) The applied incident laser light can transmit through several types of transparent media, such as air, water, glass, and plexiglass or any other transparent plastics (e.g., acrylic, polyethylene, polypropylene, polycarbonate), without significant losses.
- 3) Both crystalline and amorphous materials can be detected by Raman shift responses.
- 4) Species in aqueous solution can also be detected by confocal Raman spectroscopy if the concentration is higher than the detectable threshold [23,24].

These characteristics make *in situ* Raman spectroscopy a very promising analytical tool for the study of corrosion product layers formed at low  $\text{H}_2\text{S}$  pressures and low temperature. This is especially adaptable to marginally sour environments that have fewer safety-related complications but result in extremely thin, albeit complicated, corrosion product layers that are difficult to be identified. A properly designed system enables the Raman laser signal to go through the aqueous solution and the transparent reactor window to arrive at the surface of interest, interact with the surface layer structure, and then scatter back to the detector. Although the freshly precipitated mackinawite was usually nanocrystalline or “amorphous”, the characteristic Raman peaks can be detected [25,26].

However, the corrosion product layers formed in the marginally sour environments may contain several phases; their responses to the Raman signal must be considered and differentiated if an effective spectrum with characteristic peaks is desired. For example, carbonyl groups usually have one very strong peak at Raman shift round  $1300\text{ cm}^{-1}$ , therefore  $\text{FeCO}_3$  can be detected by this characteristic peak [27]. Iron oxides have multiple close peaks, but these peaks are not overlapping with each other. Therefore, they can be differentiated from one another.  $\text{Fe}_3\text{C}$  displays a plateau with double peaks at around  $1100\text{ cm}^{-1}$  [28,29]. Both iron sulfides (e.g., mackinawite, pyrite) and elemental sulfur are weak Raman scatterers; this makes their identification a challenge. This present work described the design and development of an *in situ* Raman cell and addressed these issues mentioned above about the proposed identification of phases formed during the corrosion process. The work also logically focuses on corrosion product layers formed in marginally sour environments.

## 2. Experimental setup and procedure

### 2.1. Experimental equipment

A Bruker confocal Raman microscope SENTERRA II was used in the experimental work. A  $\times 10$  objective with 7 mm focal length, a  $\times 50$  objective with 1 mm focal length, and a  $\times 50$  objective with 10 mm focal length were used for calibration with mineralogical specimens, *ex situ* analysis and *in situ* spectral acquisition, respectively. A He–Ne laser of 514 nm wavelength with 25 mW output power and 732 nm wavelength with 100 mW output power at backscattering mode was applied for each analysis. The confocal pinhole diameter was of  $25 \times 100\ \mu\text{m}$ . Raman

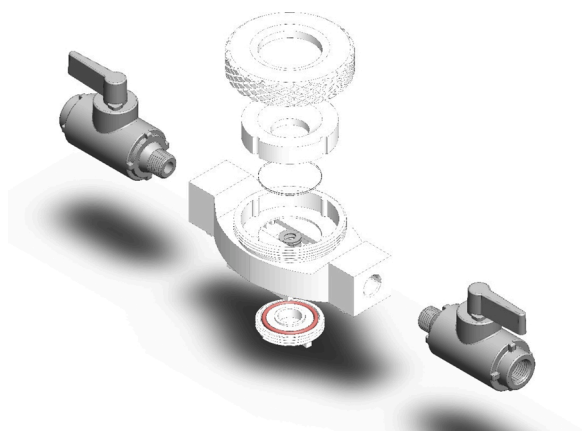


Fig. 2. *In situ* Raman flow cell (IRFC) reactor 3D sketch.

spectra were first collected in the spectral region of  $80 \sim 4000 \text{ cm}^{-1}$  with a resolution of  $4 \text{ cm}^{-1}$ , then at  $80 \sim 1600 \text{ cm}^{-1}$  with a spectra resolution of  $1.5 \text{ cm}^{-1}$  at a different spot on each sample. Spectral acquisitions required five accumulations for a good signal-to-noise ratio.

The *in situ* Raman flow cell was designed as shown by the 2D sketch in Fig. 1, which displays a cross section of the reactor. The specimen was fixed in the center of the reactor, with the fluid flowing through the reactor. The 3D sketch drawn by Solidworks is shown in Fig. 2. The specimen was inserted into a gas-tight 3D printed plastic enclosure with a sapphire window. The idea was based on the fact that glass is transparent under the Raman signal (laser).

The *in situ* Raman flow loop was designed based on the sketch shown in Fig. 3. The *in situ* Raman flow cell (IRFC) reactor was connected with two reservoirs of aqueous solutions with detachable connectors and three-way valves. The flow loop could be switched between 1) the  $30 \text{ }^\circ\text{C}$ ,  $\text{pH } 5.01 \pm 0.01$ ,  $0.97 \text{ bar CO}_2$  and  $0.04 \text{ mbar H}_2\text{S}$  saturated  $1 \text{ wt.}\%$  NaCl solution; and 2) the nitrogen saturated deionized water at  $30 \text{ }^\circ\text{C}$ . Pictures in Fig. 4 show the finished *in situ* Raman flow loop and cell.

## 2.2. Experimental procedures

The entire flow loop was rinsed with deionized water before each experiment. Two-liter  $1 \text{ wt.}\%$  NaCl solution was introduced into the system with a continuous sparging of analytical pure grade  $\text{CO}_2$  gas at  $30 \text{ }^\circ\text{C}$  under atmospheric pressure. Mixing was achieved by a rotating pedal at a speed of  $300 \text{ rpm}$ .  $\text{Na}_2\text{CO}_3$  was added to adjust the solution to  $\text{pH } 5$

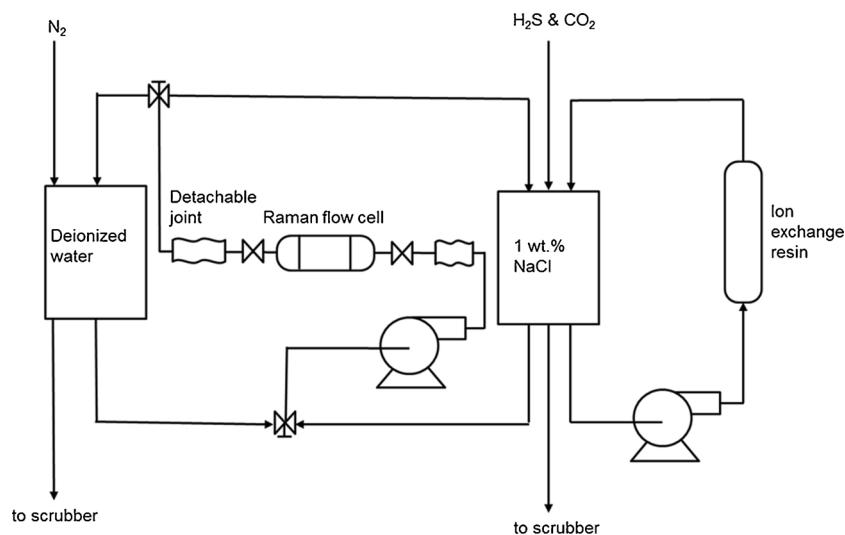


Fig. 3. P&ID of the designed *in situ* Raman flow loop.

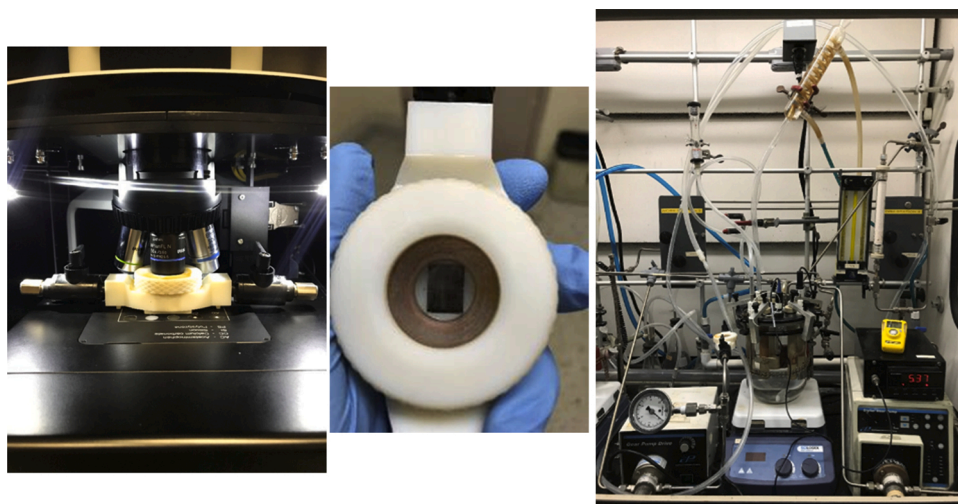


Fig. 4. Pictures of the *in situ* Raman flow cell & flow loop.

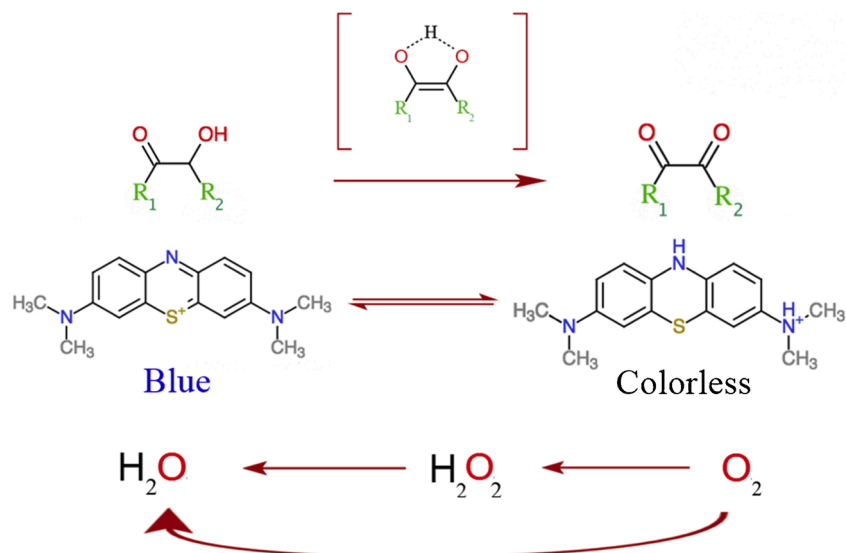
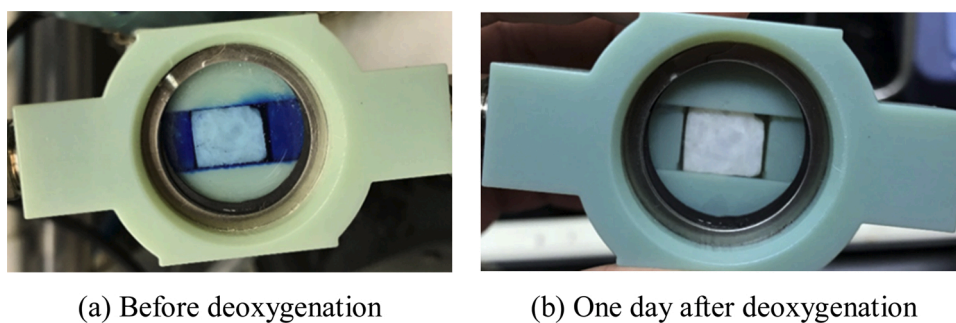


Fig. 5. Using methylene blue as an oxygen indicator to test cell tightness (*Thyphoon7979* ([https://commons.wikimedia.org/wiki/File:Complete\\_reactions\\_of\\_blue\\_bottle\\_experiment.png](https://commons.wikimedia.org/wiki/File:Complete_reactions_of_blue_bottle_experiment.png)), <https://creativecommons.org/licenses/by-sa/4.0/legalcode>) (For interpretation of the references to colour in this figure legend, the reader is referred to the web version of this article).



(a) Before deoxygenation

(b) One day after deoxygenation

Fig. 6. The sealing capacity of the IRFC.

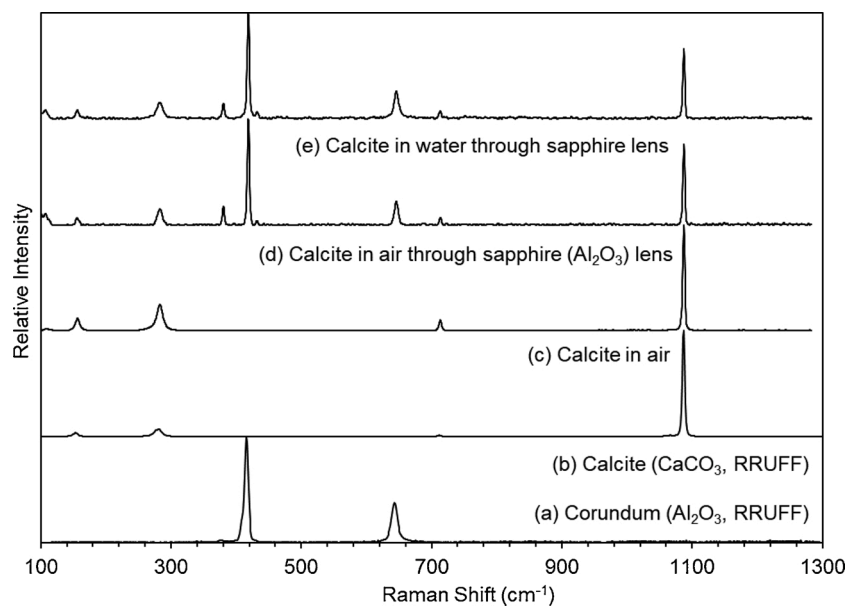


Fig. 7. Calibration of IRFC with calcite mineral standard sample ( $\times 10$  objective).

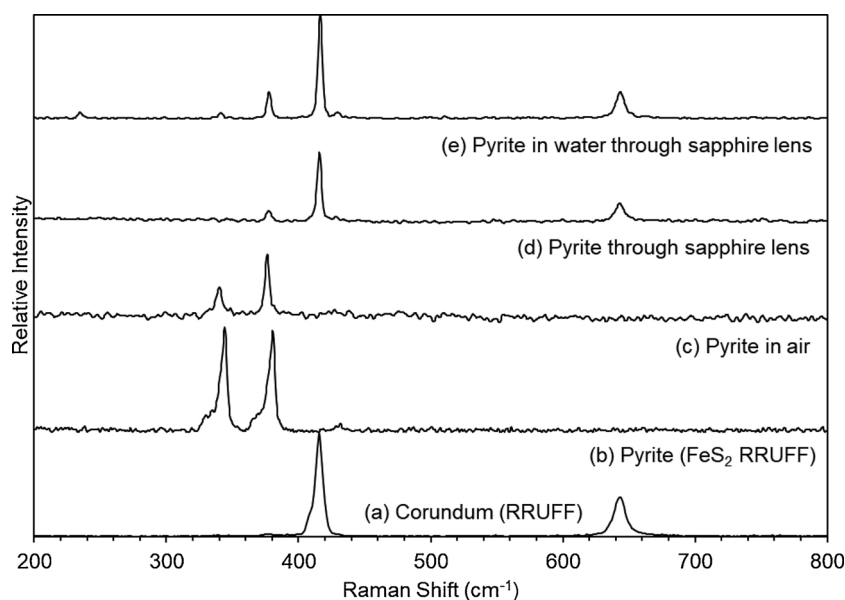


Fig. 8. Calibration of IRFC with pyrite.

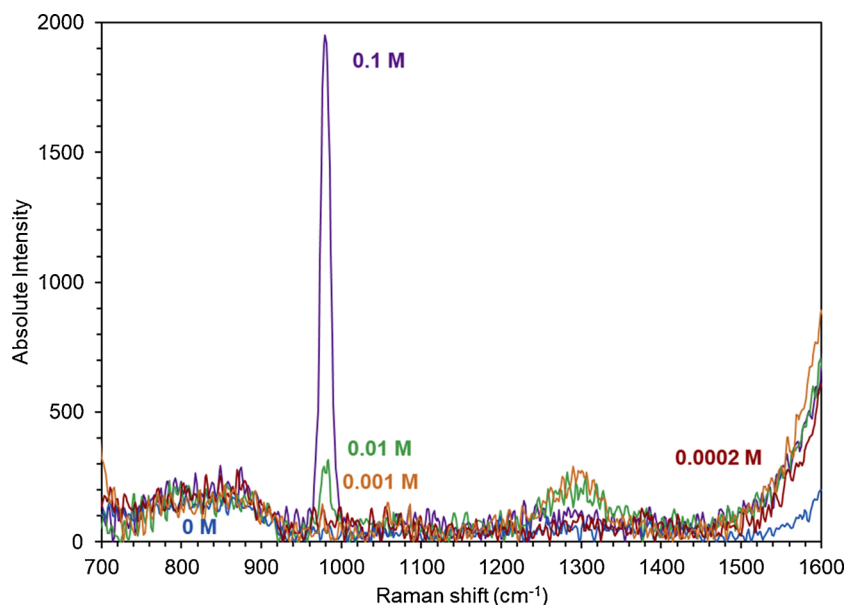


Fig. 9. Raman spectra of standard  $\text{Na}_2\text{SO}_4$  solution of various concentrations showing the characteristic peak of  $\text{Na}_2\text{SO}_4$  detectable above 0.01 mol/L.

and kept around  $5.01 \pm 0.01$  by an automatic titration system. Dissolved  $\text{O}_2$  concentration was monitored continuously by a HACH® Orbisphere 510 oxygen meter. After two hours of sparging of  $\text{CO}_2$ , an  $\text{H}_2\text{S}/\text{CO}_2$  gas mixture was added in to get a partial pressure of  $\text{H}_2\text{S}$  of 0.04 mbar. Four  $12 \text{ mm} \times 12 \text{ mm} \times 2 \text{ mm}$  API X65 steel specimens with a surface finish of 600 grit was loaded after  $[\text{O}_2]_{(\text{aq})} < 10 \text{ ppb}_{(\text{w})}$ . The specimen in the *in situ* Raman flow cell was connected into the flow loop at the same time. As the valve to the flow cell was turned on, the dry steel specimen inside the flow cell was flooded by the deoxygenated solution immediately. The corrosion experiment began. The *in situ* Raman flow cell shall be disconnected when measurement was needed.

### 3. Results and discussion

#### 3.1. Seal test of the IRFC

Methylene blue as an oxygen indicator was used together with

glucose to test whether oxygen ingress could occur inside the Raman cell after it was disconnected from the flow loop. The redox reaction, which induces the color change, is shown in Fig. 5 [30].

As shown in Fig. 6, the methylene solution is originally blue in color. After being heated to above  $40^\circ\text{C}$ , it is reduced into a colorless anoxic solution. The solution would only turn blue if exposed to oxygen. During operation, the solution remained colorless for at least one day. The threshold of color change for methylene blue is measured to be 1.3 ppm by a HACH® Orbisphere 510 oxygen meter at the gas outlet incorporated in the experimental setup. It is understood that this method is rather crude since it cannot detect dissolved oxygen content below 1.3 ppm. However, it constituted an initial pass/fail method to validate the cell design.

#### 3.2. Calibration with minerals of known structures

Bulk mineral specimens of known crystalline identity were

**Table 1**

Reported Raman peak positions for mackinawite and other relevant iron sulfur-containing phases.

Compound	Composition	1 <sup>st</sup> peak	2 <sup>nd</sup> peak	3 <sup>rd</sup> peak	4 <sup>th</sup> peak
Nanocrystal Mackinawite [26]	FeS	208	282		
Amorphous Mackinawite [37]	FeS	214	282		
Amorphous Mackinawite [38]	FeS	218	281	395	
Oxygen Pre-corroded Mackinawite [42]	FeS	254	302	362	
Mackinawite (This work)	FeS	218	284	395	
Pyrrhotite [43]	Fe <sub>(1-x)</sub> S	326	376		
Greigite [44]	Fe <sub>3</sub> S <sub>4</sub>	248	345		
Goethite [45]	α-FeO(OH)	300	390		
Lepidocrocite [26,46]	γ-FeO(OH)	250	380	525	
Magnetite [47]	Fe <sub>3</sub> O <sub>4</sub>	297	523	666	
Hematite [48,49]	Fe <sub>2</sub> O <sub>3</sub>	223	289	404	1310
Maghemite [50]	Fe <sub>2</sub> O <sub>3</sub>	377	510	670	715
Cementite (Cohenite) [51]	Fe <sub>3</sub> C	1360	1580		
Elemental sulfur [52]	S <sub>8</sub>	154	220	473	
Siderite [53]	FeCO <sub>3</sub>	188	290	732	1087

introduced into the Raman cell to verify that they could be successfully identified during normal operating conditions. The cell was first tested with calcite because calcite has a hugely prominent intense peak of a carbonyl group (C=O in carbonate), which is expected to be easily detectable through a sapphire lens, given the consideration that sapphire itself might contribute to the background signal on the Raman spectrum under lower magnification objective with a longer focal length. The calibration result by  $\times 10$  objective is shown in Fig. 7. From bottom to top: the first (a) and second (b) spectra are reference data of calcite and corundum (sapphire window), respectively, from the RRUFF™ database (American Mineralogist Crystal Structure Database); the third spectrum (c) is commercially available calcite mineral in air, directly exposed to the laser; the fourth spectrum (d) is calcite inside the IRFC; the fifth spectrum (e) is with deionized water injected into the IRFC with the calcite. The fourth spectrum (d) shows that both the lens and the sample signal were picked up in the spectrum when the  $\times 10$  objective was used. With the two characteristic peaks of corundum near  $400\text{ cm}^{-1}$  and  $600\text{ cm}^{-1}$  labeled and subtracted, the Raman spectrum appears just as it would without the lens. The fifth spectrum (e) shows that water does not add extra peaks below a Raman shift of  $1300\text{ cm}^{-1}$ , where the inorganic bond movement relating to corrosion products and scales is located. Since the focusing length of the  $\times 10$  objective is ca. 7 mm in this case, the optical system failed to focus on the different horizontal heights. Therefore, the structural information from the lens, the

sample, and the media in between were combined in one spectrum. If an objective of higher magnification and longer working focal length is applied, and the confocal function at different heights is enabled, the sample information could be separated from the media and the lens.

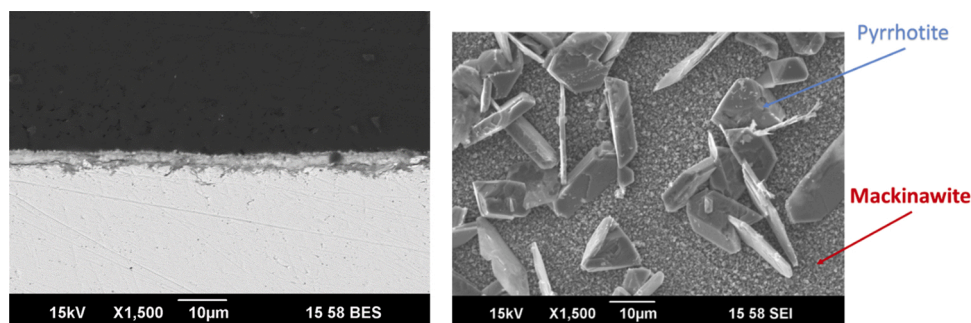
After calibration with calcite, which takes advantage of strong intensity of the signal, pyrite was tested to check for smaller signal intensity (compared to corundum) and whether Raman fluorescence would be a concern of the IRFC. The calibration result is shown in Fig. 8. From bottom to the top, the first (a) and second (b) spectra are references from the RRUFF™ database of pyrite and corundum, respectively; the third spectrum (c) was acquired from a commercially available pyrite mineral in air, directly exposed to the laser; the fourth (d) spectrum was pyrite inside the IRFC; the fifth (e) spectrum was acquired after deionized water was injected into the IRFC with the pyrite. Although the peak intensity of pyrite was small compared with that of corundum, as shown in the fourth spectrum, a very good focus facilitated by water made it detectable, as shown in the fifth spectrum. Pyrite is not as easily oxidized in air near room temperature as has been stated elsewhere [31], nor was it oxidized immediately after being in contact with water in air.

### 3.3. Detection of sulfate species with *in situ* Raman

As shown above, the Raman cell showed promising results with identifying bulk minerals bulk. It can also be used to detect specific chemicals present at small concentration in a solvent. This is of prime interest for the research reported in this H<sub>2</sub>S corrosion related work since it could potentially be used to detect products of H<sub>2</sub>S oxidation (*i.e.* sulfate species). Consequently, a series of a calibration tests were performed to explore the resolution limit for SO<sub>4</sub><sup>2-</sup> detection. As shown in Fig. 9, different concentrations of Na<sub>2</sub>SO<sub>4</sub> could influence the intensity of its characteristic peak near  $980\text{ cm}^{-1}$  [32]. However, the detection limit for Na<sub>2</sub>SO<sub>4</sub> is 0.01 mol/L, which may be too high to be truly useful. For instance, water chemistry calculation shows that at baseline condition (30 °C, 1 wt. % NaCl, pH  $5.01 \pm 0.01$ , 0.97 bar CO<sub>2</sub> and 0.04 mbar H<sub>2</sub>S), the HCO<sub>3</sub><sup>-</sup> concentration is 0.002 mol/L, and the dissolved H<sub>2</sub>S concentration is  $3.7 \times 10^{-6}$  mol/L. Therefore, it is unlikely that sulfate solute will be detected in *in situ* Raman spectra in the sour corrosion experiments. Although there is 0.17 mol/L NaCl in the solution, neither Na<sup>+</sup> nor Cl<sup>-</sup> can be detected by Raman spectroscopy as they are simple, rather than polyatomic, ions [24]. NaCl could affect the position of H<sub>2</sub>O's characteristic peak near  $3500\text{ cm}^{-1}$ , but this information is not helpful in corrosion studies.

### 3.4. Possible oxidation products of mackinawite

Raman spectroscopy uses an inelastic scattering of monochromatic light to detect vibrational, rotational, and other low-frequency modes.



(a) SEM of cross section of the layers.

(b) SEM shows pyrrhotite on top of mackinawite

Fig. 10. SEM analysis of the thick mackinawite layers.

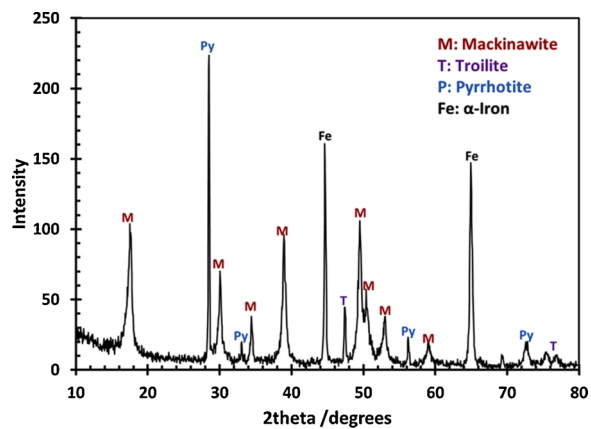


Fig. 11. XRD analysis of the layer showing both mackinawite and pyrrhotite.

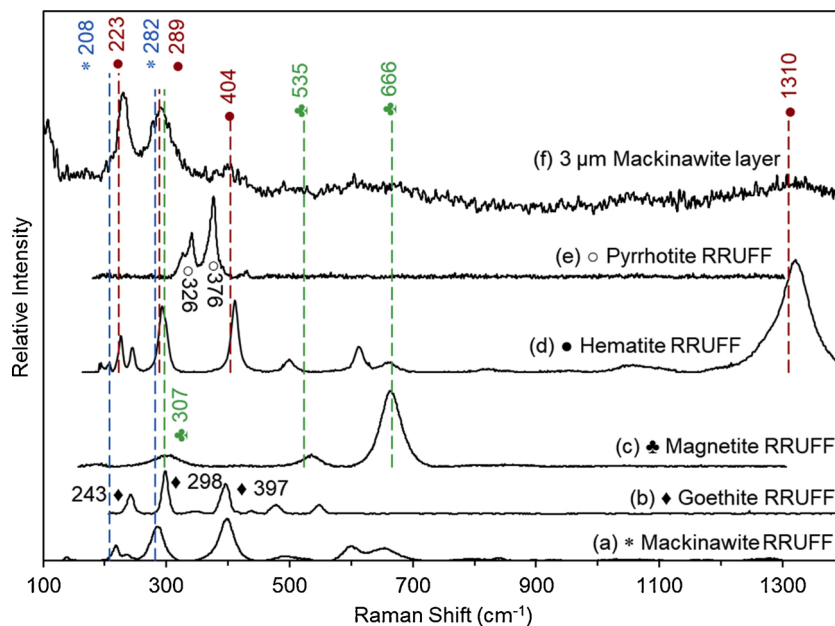


Fig. 12. Ex situ Raman spectra of the 3 μm thick mackinawite/pyrrhotite corrosion product layer and comparison with RRUFF data.

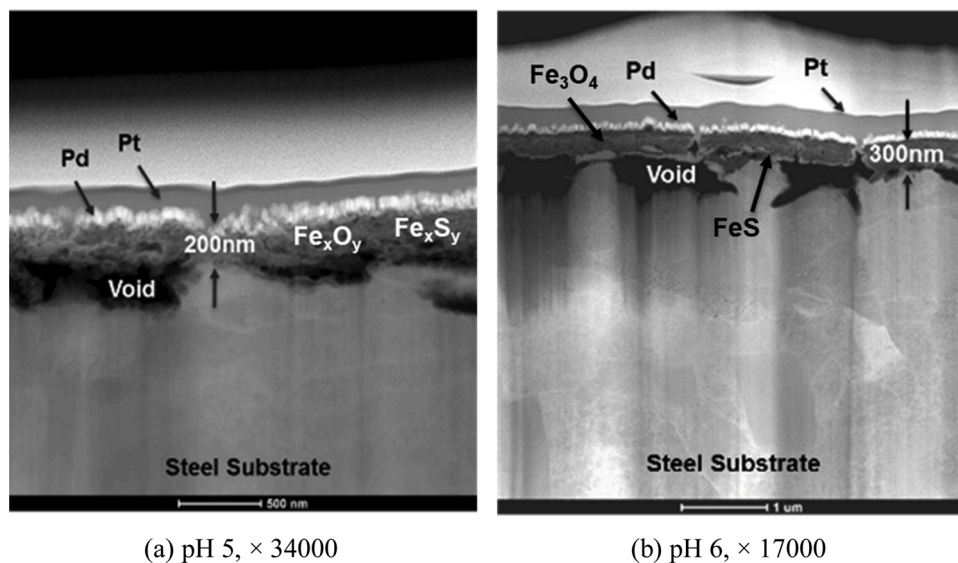


Fig. 13. TEM images of the cross section cut out by FIB from the specimen of pH 5 and pH 6 experiments (30 °C, 0.97 bar CO<sub>2</sub>, 0.04 mbar H<sub>2</sub>S, X65, 1 wt.% NaCl, 300 rpm, 7 days, [O<sub>2</sub>]<sub>aq</sub> = 20 ppb<sub>(w)</sub>).

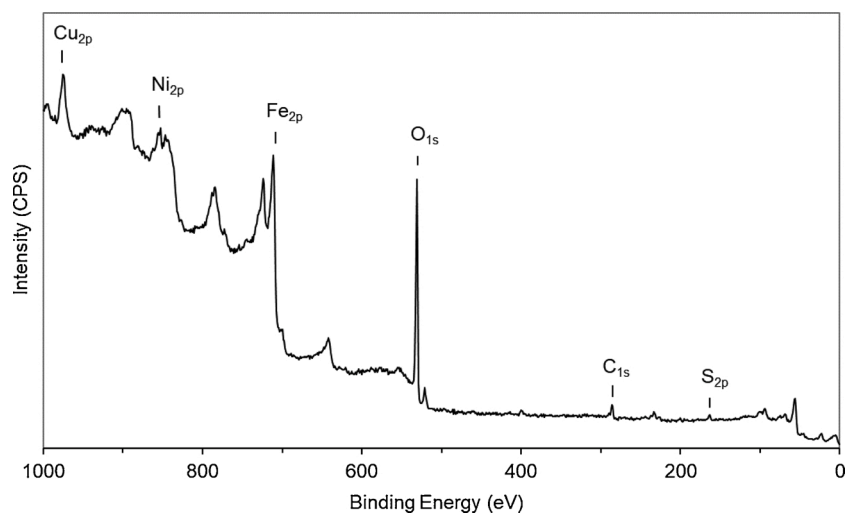


Fig. 14. XPS results—the elemental composition of the corrosion product layers.

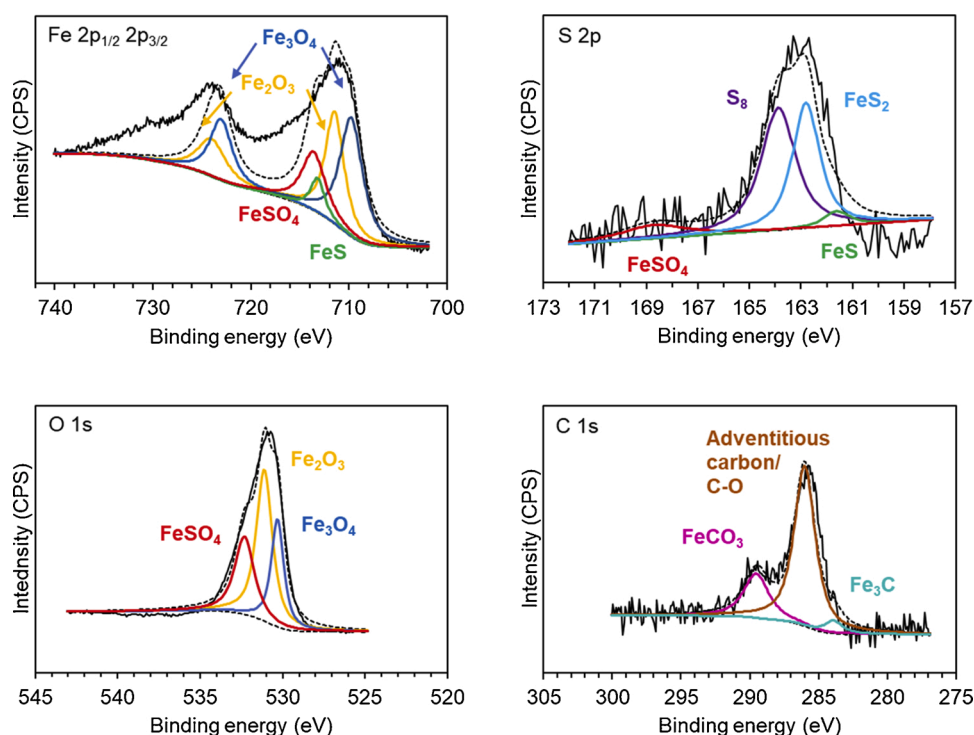


Fig. 15. XPS spectra of X65 specimens exposed to the pH 6 condition (X65, 30 °C, 0.04 mbar H<sub>2</sub>S and 0.97 bar CO<sub>2</sub>, pH 6.01 ± 0.01, 1 wt.% NaCl, 300 rpm, 7 days).

One of the unique merits of this method is that Raman spectroscopy can be applied through water and through glass, which makes analysis of the material through a specialized holder possible. It is understood that mackinawite is vulnerable to oxidation in air, especially considering laser heating effects, as well as traces of dissolved oxygen in the H<sub>2</sub>S aqueous solution. However, *ex situ* Raman spectroscopy cannot tell whether the oxidation of mackinawite happened during the corrosion tests or post-processing [19]. Therefore, the optimal option is to apply *in situ* Raman spectroscopy in an anaerobic environment to prevent oxidation.

There are many possible oxidation products of mackinawite and it is worth investigating what phases could be expected. Reported oxidation products of mackinawite include greigite [33,34], elemental sulfur, magnetite [26,35], goethite ( $\alpha$ -FeO(OH)), and lepidocrocite ( $\gamma$ -FeO(OH)) [25]. Greigite was deemed as an intermediate oxidation product, which converts into oxides and elemental sulfur over a period of time

[35]. In addition, hematite ( $\alpha$ -Fe<sub>2</sub>O<sub>3</sub>) and maghemite ( $\gamma$ -Fe<sub>2</sub>O<sub>3</sub>) have been reported as oxidation products of mackinawite [25]. It has been found [26] that mackinawite oxidation does not necessarily mean that a new phase will be detected. Fe (III) has been reported to incorporate into the tetrahedral sites of mackinawite [36] and will not be detected as a new phase if its content is lower than 20 % [37].

One of the challenges facing this study is that the standard database of iron sulfides for Raman spectra is in places sparse and incomplete. Generally speaking, the nanocrystalline [26], amorphous [37,38], or partially oxidized mackinawite [26,39] all have distinct peaks, shifted peaks, or broadened peaks as compared to a well-crystallized mackinawite [26]. Typical Raman shift peak positions for mackinawite and its oxidation products are summarized in Table 1. According to Bourdoiseau et al., [26], freshly synthesized nanocrystalline mackinawite has two peaks, one at 208 cm<sup>-1</sup>, which corresponds to its lattice mode [40]; and another at 281~298 cm<sup>-1</sup>, which is the symmetric stretching mode

**Table 2**  
Binding energies for compounds found on the surface of corroded mild steels.

Compound	Fe 2p		S 2p		O 1 s	C 1 s
	Fe 2p <sub>3/2</sub>	Fe 2p <sub>1/2</sub>	S 2p <sub>3/2</sub>	S 2p <sub>1/2</sub>		
Fe <sub>2</sub> O <sub>3</sub>	709.90	724.00			529.50	
	[54] ~ 711.60	[56]			[57] ~ 531.95	
	[55]				[58]	
Fe <sub>3</sub> O <sub>4</sub>	708.10	723.50			529.10	
	[59] ~ 711.40	[56]			[61] ~ 530.70	
	[60]				[62]	
FeOOH	711.00	724.30			530.10	
	[60] ~ 711.80	[56]			[59] ~ 531.80	
	[63]				[60]	
FeS	710.30		160.80			
	[64], 712.20		[67], 161.40			
	[65], 713.60		[65]			
	[66]					
				<b>162.23</b> [68]		
FeS <sub>2</sub>	706.60		<b>162.20</b>	<b>163.50</b>		
	[65] ~ 708.60		[70], <b>162.80</b>	[72]		
	[69]		[71], <b>164.00</b>			
S <sub>8</sub>			<b>163.60</b>			
			[71], <b>164.00</b>			
			[73]			
FeSO <sub>4</sub>	713.60		168.70		532.30	
	[66]		[74], 168.80		[74]	
			[66]			
Fe <sub>2</sub> (SO <sub>4</sub> ) <sub>3</sub>			168.00		531.60	
			[59], 169.10		[74], 532.20	
			[74]		[59]	
FeCO <sub>3</sub>					289.40	
Fe <sub>3</sub> C	708.10				283.60	
	[76]				[77], 283.90	
					[76]	
C-O-C					<b>286.00</b> [78]	

of FeS [26]. Further, the degree of crystallinity will change the latter, not the former. The 208 cm<sup>-1</sup> peak shifts to 214~218 cm<sup>-1</sup> in amorphous mackinawite, and even shifts to 254 cm<sup>-1</sup> in the case where the specimen is first pre-corroded aerobically before sulfide is added. However, a careful comparison between some of the *in situ* Raman spectra [25,26] with other *ex situ* Raman spectra [37,38,41] reveals that hematite is commonly mistakenly labeled as mackinawite. Simply put, any “mackinawite” spectrum that includes peaks other than 208 cm<sup>-1</sup> (1st peak in Table 1) and 282 cm<sup>-1</sup> (2nd peak in Table 1), like 395 cm<sup>-1</sup> (3rd peak in Table 1) or 1310 cm<sup>-1</sup> (4th peak in Table 1), does not identify mackinawite but is representative of its oxidation.

### 3.4.1. *Ex situ* Raman spectra of thick mackinawite/pyrrhotite layer formed at high H<sub>2</sub>S partial pressure

*Ex situ* Raman spectroscopy was used to analyze both thick and thin layers in order to verify if the corrosion product layers have been oxidized after being retrieved from the reactor and dried. Later, it will be compared with the *in situ* Raman spectra.

First, a thick FeS layer formed on C1018 steel and prepared at 80 °C under 2 bar H<sub>2</sub>S, pH 4.0, 1 wt.% NaCl for 2 weeks, was analyzed by *ex situ* Raman spectroscopy. Fig. 10. shows the thickness of the layer is about 3 μm (a), with scattered pyrrhotite crystals on top of mackinawite (b).

Fig. 11 shows the XRD analysis of the layer confirming both mackinawite and pyrrhotite were present. This analysis was performed immediately after the specimen was retrieved from the reactor. Therefore, no sign of oxidation was found.

Fig. 12 compares two Raman spectra of the corroded C1018 steel specimen with a 3 μm thick mackinawite/pyrrhotite layer, with related RRUFF™ database spectra. This specimen was the same one that was characterized by XRD but was exposed to air for a significant time before Raman analysis was performed. Both mackinawite and hematite were identified in the Raman spectra, although mackinawite seemed to be dominant. Here the mackinawite qualitatively corresponds to the bulk of the layer composition. However, the pyrrhotite crystals could not be detected by Raman analysis, possibly because they were too scattered on the surface and because the location of the analysis missed them; Raman microscopy (laser spot size 0.5 ~ 10 μm) yields spectra from an area orders of magnitude smaller than XRD (spot size > 20 μm).

### 3.4.2. *Ex situ* Raman spectra of thin mackinawite layers formed at low H<sub>2</sub>S partial pressure

The analysis was repeated *ex situ* on a much thinner layer. Two experimental conditions were chosen: 1) 30 °C, pH 5.01 ± 0.01, 0.97 bar CO<sub>2</sub>, 0.04 mbar H<sub>2</sub>S, 300 rpm stir bar, 7 days, [O<sub>2</sub>]<sub>(aq)</sub> ≈ 20 ~ 40 ppb<sub>(w)</sub>; 2) 30 °C, pH 6.01 ± 0.01, 0.97 bar CO<sub>2</sub>, 0.04 mbar H<sub>2</sub>S, 300 rpm stir bar, 7 days, [O<sub>2</sub>]<sub>(aq)</sub> ≈ 20 ~ 40 ppb<sub>(w)</sub>. The corrosion product layers formed under these two conditions were typically porous, existing as a ca. 200 nm thick mixture of iron sulfide and iron oxide. Neither XRD nor SAED could provide precise diffraction patterns of these nanolayers [18]. SAED could identify the outer layer at pH 6 as magnetite, the inner layer was mistakenly matched with Fe<sub>0.91</sub>S [18]. PED made the correct diffraction mapping match as mackinawite (FeS) [18]. Fig. 13 summarizes these layers' structural information and compares them.

Besides TEM-EDS, XPS was also applied to the specimen generated at the pH 6 condition (X65, 30 °C, 0.04 mbar H<sub>2</sub>S, and 0.97 bar CO<sub>2</sub>, pH 6.01 ± 0.01, 1 wt.% NaCl, 300 rpm, 7 days). As Fig. 14 shows, Fe, S, O, C are the elements of concern. Fig. 15 shows that iron sulfide and oxide were detected, which agrees with the FIB-TEM results. Both Fe 2p and O 1s confirmed the existence of Fe<sub>2</sub>O<sub>3</sub> and Fe<sub>3</sub>O<sub>4</sub>. As for S 2p, the result suggests that S<sup>2-</sup> has been oxidized. However, the valence states of the oxidation product cannot be confirmed: it could be S-, S° or SO<sub>4</sub><sup>2-</sup>. The problem is that if FeS, FeS<sub>2</sub>, FeSO<sub>4</sub> were added into the peak fitting in Fe 2p, a fit of the sum of the peaks can be achieved almost all the time, especially given the broadening of the Fe 2p<sub>3/2</sub> and sp<sub>1/2</sub> peaks. Moreover, C 1s shows the sign of potential coexistence of FeCO<sub>3</sub> and Fe<sub>3</sub>C in the corrosion product layer.

The peak fitting results in Fig. 15 were based on the literature binding energies listed in Table 2. It is easily detectable that binding energies for some compounds are very close to each other. That is the reason why a fit can be easily achieved with multiple possibilities. Although characteristic peaks of different elements in the same compounds can be compared with each other to enable a mutual confirmation, it is still difficult to make sure the fingerprint of each compound is fully determined.

The sampling depth of the XPS is very limited compared with FIB-TEM. Therefore, the sample could not be plated with any protective layer such as Au or Pd for preservation before transferring to the XPS sampling chamber. Although the samples had been sputtered to remove contamination, whether this procedure was completely effective to remove *ex situ* oxidation products is unknown. Consequently, whether the oxyhydroxide or oxide was generated *in situ* or *ex situ* cannot be unequivocally determined with this method. Therefore, XPS is not an ideal tool in terms of layer analysis in sour corrosion studies when specimen oxidation is expected.

In Fig. 16, the Raman spectra of both pH 5 (baseline condition) and pH 6 specimens were compared with the RRUFF database spectra of all the possible oxidation products of iron sulfides. The curve (f) is the Raman spectra of a corroded X65 steel specimen with a 200 nm porous

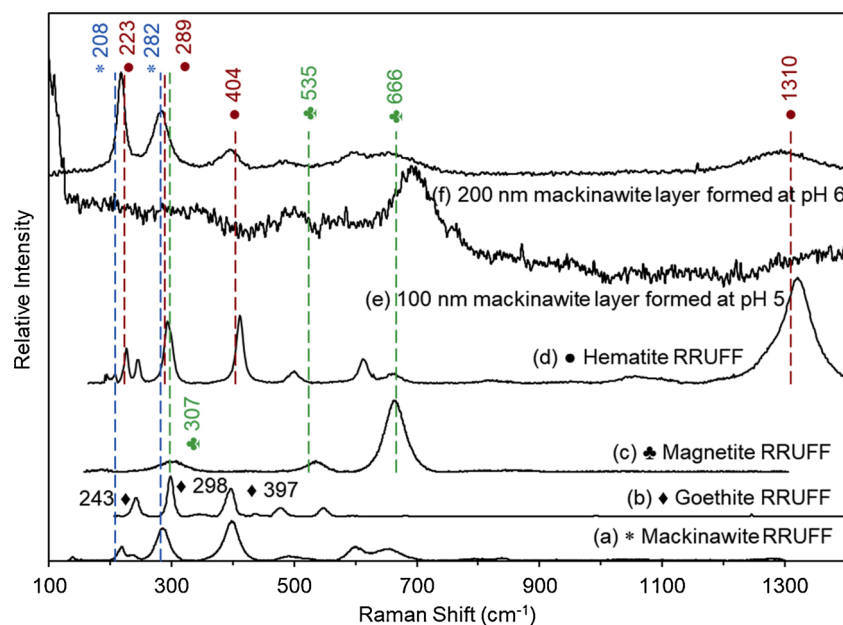


Fig. 16. *Ex situ* Raman spectra of the thin mackinawite corrosion product layer and comparison with RRUFF data.

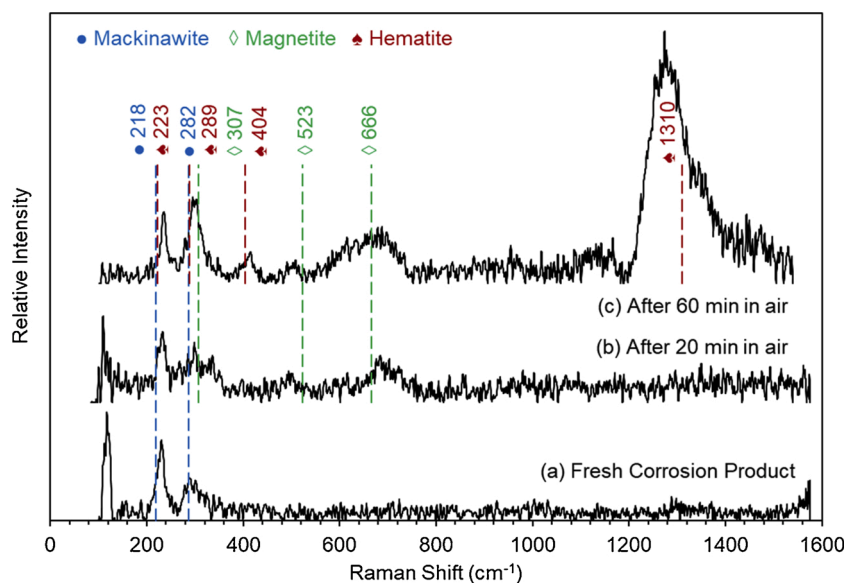


Fig. 17. Oxidation of mackinawite with time measured with a Raman microscope (laser excitation line 532 nm, power 25 W, the specimens were corroded at 30 °C, pH 5.01 ± 0.01, 0.97 bar CO<sub>2</sub>, 0.04 mbar H<sub>2</sub>S, 300 rpm stir bar, 7 days, [O<sub>2</sub>]<sub>(aq)</sub> ≈ 20 ~ 40 ppb<sub>(w)</sub>).

corrosion product layer, according to FIB-TEM analysis. A possible combination of mackinawite and hematite fits spectrum (f), because: 1) the first peak of curve (f) from the left could be explained by an overlap between 218 cm<sup>-1</sup> (mackinawite) and 223 cm<sup>-1</sup> (hematite, Fe<sub>2</sub>O<sub>3</sub>); 2) the second peak of curve (f) could be an overlap with mackinawite at 282 cm<sup>-1</sup>, hematite at 289 cm<sup>-1</sup>, and goethite at 298 cm<sup>-1</sup>; 3) plateaus near the Raman peaks at 404 cm<sup>-1</sup> and 1310 cm<sup>-1</sup> belong to hematite only. On the other hand, only magnetite can be identified in the “baseline pH 5” spectrum (e) by the peak near 666 cm<sup>-1</sup>, which indicates the mackinawite has been oxidized. The mackinawite peaks failed to be detected on spectrum (e). Again, this agrees with the previous findings based on TEM (Fig. 13) that the baseline corrosion product layer was very thin and porous; the uneven surface of this layer returns weak signals. Compared to the layers formed at pH 5, the morphological features formed at pH 6 seem more ordered, which echoes the TEM-SAED findings (Fig. 13) once again. However, it is

noteworthy that the mackinawite formed at pH 5 was oxidized into magnetite, while the similar layer formed at pH 6 was oxidized into hematite.

### 3.4.3. Oxidation route of mackinawite in the air (converted from magnetite to hematite with time)

In order to determine the oxidation route of mackinawite, another *ex situ* Raman analysis (Fig. 17) was performed on a freshly retrieved and dried specimen from a corrosion experiment at the baseline condition (30 °C, pH 5.01 ± 0.01, 0.97 bar CO<sub>2</sub>, 0.04 mbar H<sub>2</sub>S, 300 rpm stir bar, 7 days, [O<sub>2</sub>]<sub>(aq)</sub> ≈ 20 ~ 40 ppb<sub>(w)</sub>). This first scan (a) of this specimen shows that the mackinawite in the layer had not yet been oxidized; the second scan performed 20 min later on a different spot shows that the mackinawite had been partially oxidized into magnetite; while the third scan performed 40 min later on another spot suggests that the mackinawite was finally converted into hematite. Therefore, the oxidation

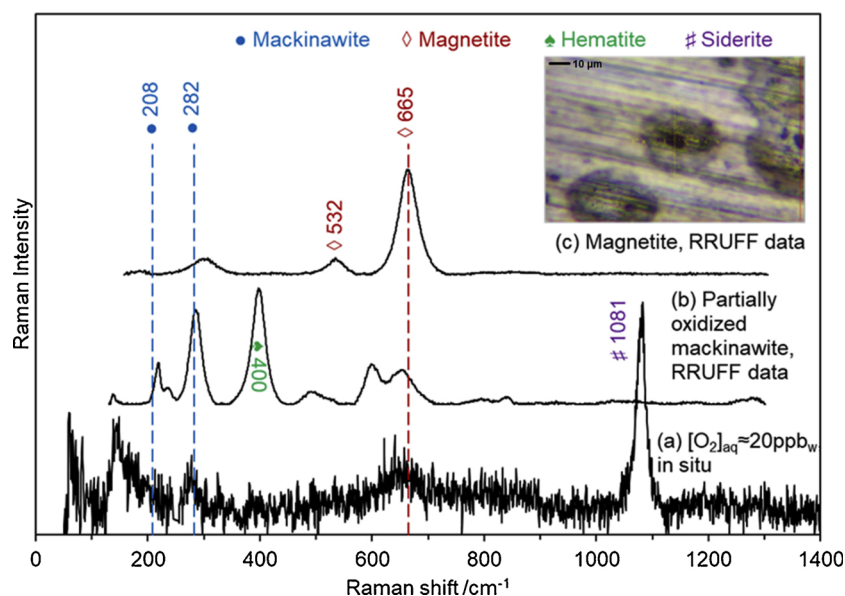


**Fig. 18.** *In situ* Raman spectroscopy analysis: direct proof of oxidation of mackinawite into magnetite in the aqueous solution on a corroding surface (baseline condition at 30 °C, pH  $5.01 \pm 0.01$ , 0.97 bar CO<sub>2</sub>, 0.04 mbar H<sub>2</sub>S, 300 rpm stir bar, 7 days, with [O<sub>2</sub>]<sub>aq</sub> = 3~20 ppb<sub>(w)</sub>). Spectrum (a) is taken after 4 days exposure. The Raman microscopy image in Fig. 18 shows several pits with diameters around 10 μm.

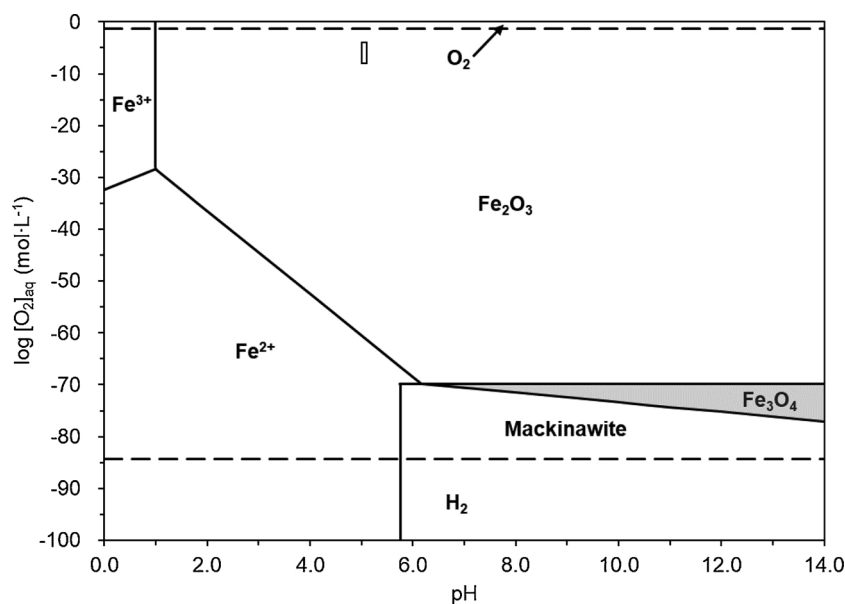


**Fig. 19.** Phase equilibrium diagram of Mackinawite-O<sub>2</sub>-H<sub>2</sub>O system (298.15 K, 1 atm, pH<sub>2</sub>S = 0.04 mbar (40 ppm<sub>v</sub>)). The small rectangle ([O<sub>2</sub>]<sub>aq</sub> = 10<sup>-8</sup> ~ 10<sup>-4</sup> mol/L, pH = 5.00 ~ 5.10) in the diagram is the baseline condition in terms of localized corrosion in marginally sour environments.

route of mackinawite in the air appears to be as follows: mackinawite  $\rightarrow$  magnetite  $\rightarrow$  hematite.

### 3.5. *In situ* test result on precipitated mackinawite layer

Since mackinawite is extremely sensitive to oxidation in post-processing (drying process and storage), as shown by previous studies on thick, thin and freshly retrieved corrosion product layers (Figs. 12, 16, and 17), *in situ* Raman is probably the only way to show the original status of the mackinawite corrosion product layers in marginally sour corrosion. Therefore, a 7 day corrosion experiment was performed at the baseline conditions (30 °C, pH  $5.01 \pm 0.01$ , 0.97 bar CO<sub>2</sub>, 0.04 mbar H<sub>2</sub>S, 300 rpm stir bar, 7 days, [O<sub>2</sub>]<sub>aq</sub>  $\approx$  3 ~ 20 ppb<sub>(w)</sub>), [19,20]. *In situ* Raman analysis was done every day to investigate the formation and

transformation (*i.e.*, oxidation) of corrosion product layers. As shown in Fig. 18, after four days of exposure, the *in situ* Raman spectrum of the corrosion product layer shows that mackinawite has been partially oxidized into magnetite due to the presence of 7 ppb<sub>(w)</sub> of dissolved O<sub>2</sub>. This finding reveals that O<sub>2</sub> could still affect H<sub>2</sub>S corrosion, if there are traces of dissolved O<sub>2</sub> (>3 ppb<sub>(w)</sub>). When continuously sparged with gases such as H<sub>2</sub>S, CO<sub>2</sub>, and/or N<sub>2</sub>, O<sub>2</sub> could still effectively impact this corrosion system. It was hypothesized that the initiation of pitting is due to the partial oxidation of the FeS layer. This hypothesis has been verified by the observation that no pitting was detected at O<sub>2</sub> content below 3 ppb<sub>(w)</sub> [19,20]. The Raman microscopy image in Fig. 18 shows several pits with diameters around 10 μm.

Oxidation of mackinawite is a spontaneous process with the presence of extremely low O<sub>2</sub> contamination. A phase equilibrium diagram of the

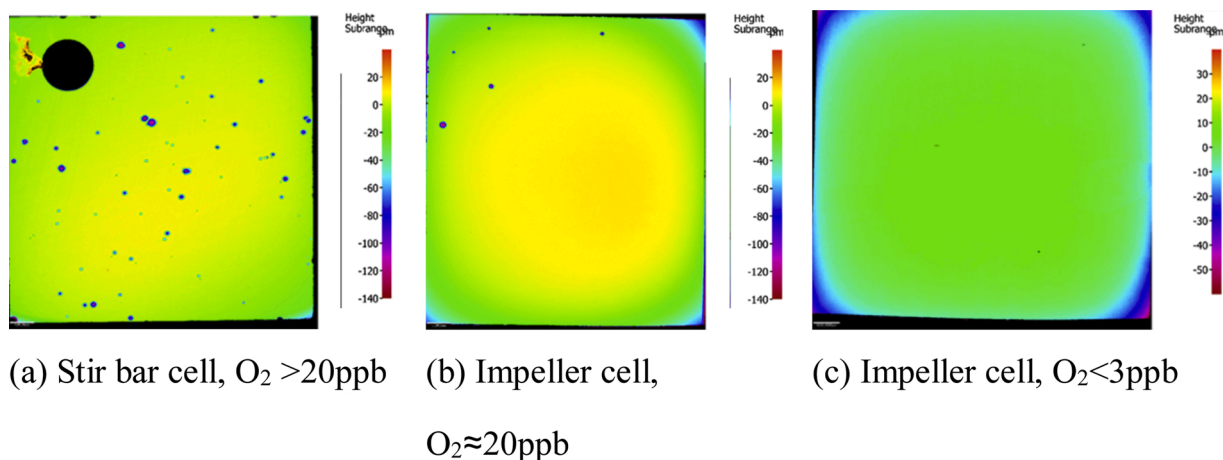


Fig. 20. Surface profilometry image after layer removal. (the specimens were corroded at 30 °C, pH 5.01 ± 0.01, 0.97 bar CO<sub>2</sub>, 0.04 mbar H<sub>2</sub>S, 300 rpm stir bar, 7 days).

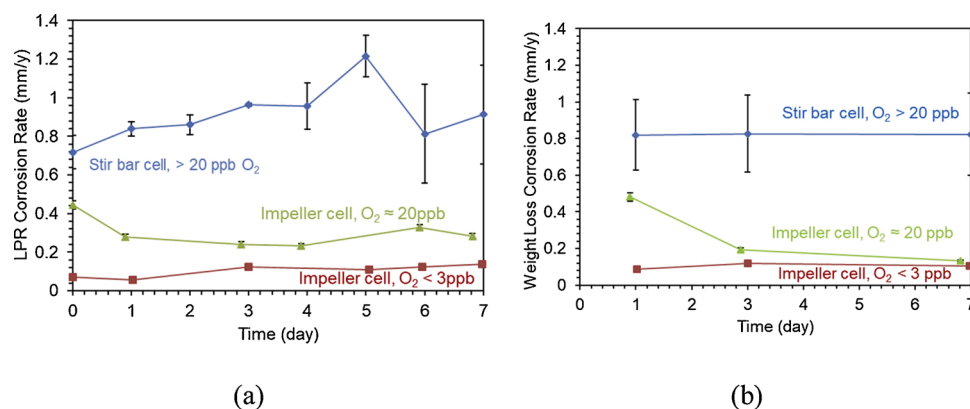


Fig. 21. Linear polarization resistance (a) and weight loss (b) corrosion rate (the specimens were corroded at 30 °C, pH = 5.01 ± 0.01, pCO<sub>2</sub> = 0.97 bar, pH<sub>2</sub>S = 0.04 mbar, 300 rpm stir bar, 7 days).

Mackinawite-O<sub>2</sub>-H<sub>2</sub>O system (298.15 K, 1 atm, pH<sub>2</sub>S = 0.04 mbar (40 ppm<sub>v</sub>)) is presented in Fig. 19. The thermodynamic data used is derived from the literature and handbook [79–81]. The small rectangle ([O<sub>2</sub>]<sub>aq</sub> = 10<sup>-8</sup> ~ 10<sup>-4</sup> mol/L (e.a. 3~20 ppb<sub>w</sub>), pH = 5.00 ~ 5.10) in the diagram is the baseline condition in terms of localized corrosion in marginally sour environments. This diagram shows that oxidation of mackinawite should be able to happen with even [O<sub>2</sub>]<sub>aq</sub> < 3 ppb<sub>w</sub> thermodynamically. Although it is not kinetically significant enough to initiate pitting at the baseline condition during the 7-day experiments.

### 3.6. In situ test result on chemisorbed S<sub>ads</sub>(Fe) layer

Corrosion experiments at baseline conditions with different levels of dissolved oxygen were performed to verify the finding that oxygen induces pitting corrosion in marginally sour environments. As a reminder, neither a corrosion product layer nor pitting was found during the 7 days experiments with [O<sub>2</sub>]<sub>aq</sub> < 3 ppb<sub>w</sub>, as shown in the FIB-TEM [18] and IFM results (Fig. 20). However, as shown in Fig. 21, one phenomenon worth noting is that this “layer-free” steel surface featured a relatively very low corrosion rate at 0.09 mm/y compared with other conditions where a thick layer could be observed [18]. Therefore, it was speculated that a chemisorbed S<sub>ads</sub>(Fe) layer [82] had formed and was responsible for this lower corrosion rate and pitting-free result. It is a challenge for Raman observation given the assumption that the S<sub>ads</sub>(Fe) is akin to a monomolecular layer.

It is important to note that maintaining a dissolved O<sub>2</sub> content below 3 ppb<sub>w</sub> is a challenge due to the complex flow loop design, which

involves multiple connectors that brings additional O<sub>2</sub> diffusion. Therefore, the best effort to control ingress of oxygen could only achieve about a [O<sub>2</sub>]<sub>aq</sub> = 5 ~ 7 ppb<sub>w</sub> average during the 7-day experiment at the baseline conditions with the flow loop. [O<sub>2</sub>]<sub>aq</sub> < 3 ppb<sub>w</sub> for 7 days is only achievable repeatedly without a flow loop. The surface condition of the corroding X65 steel specimens under the naked eye and microscope after 1, 3 and 7 days are shown in Fig. 22. It shows that basically, the steel surface remained shiny in the first three days, while signs of formation of a precipitated layer were apparent after seven days of exposure. This is because [O<sub>2</sub>]<sub>aq</sub> reached 7 ppb<sub>w</sub> at that point, compromising the chemisorbed layer and leading to a surface saturation of FeS larger than unity.

As shown in Fig. 23, *in situ* and *ex situ* Raman spectra of the corroding surface at the baseline condition with [O<sub>2</sub>]<sub>aq</sub> = 5 ~ 7 ppb<sub>w</sub> after 1, 3, and 7 days of exposure were compared with each other. The main result is that no clear product of mackinawite oxidation could be identified in the *in situ* analysis, yet the presence of mackinawite could also not be confirmed. The Raman peaks on the *in situ* Raman spectra were not prominent compared with the noisy background, probably due to the attenuation of the laser signals with the longer focal length or the aqueous solution as the transmission medium. In contrast, the *ex situ* Raman spectra (line g, k and m) identified mackinawite but also magnetite. The *in situ* Raman spectra show a relatively strong peak around 150~200 cm<sup>-1</sup>, which could be the possible match of bending or torsion vibration modes of the S—S bond in elemental sulfur (S<sub>8</sub>). The literature [83] shows that the vibrations in the spectra of S<sub>8</sub> molecule appear as regions of stretching (ν, 400–475 cm<sup>-1</sup>), bending (δ, 152–267

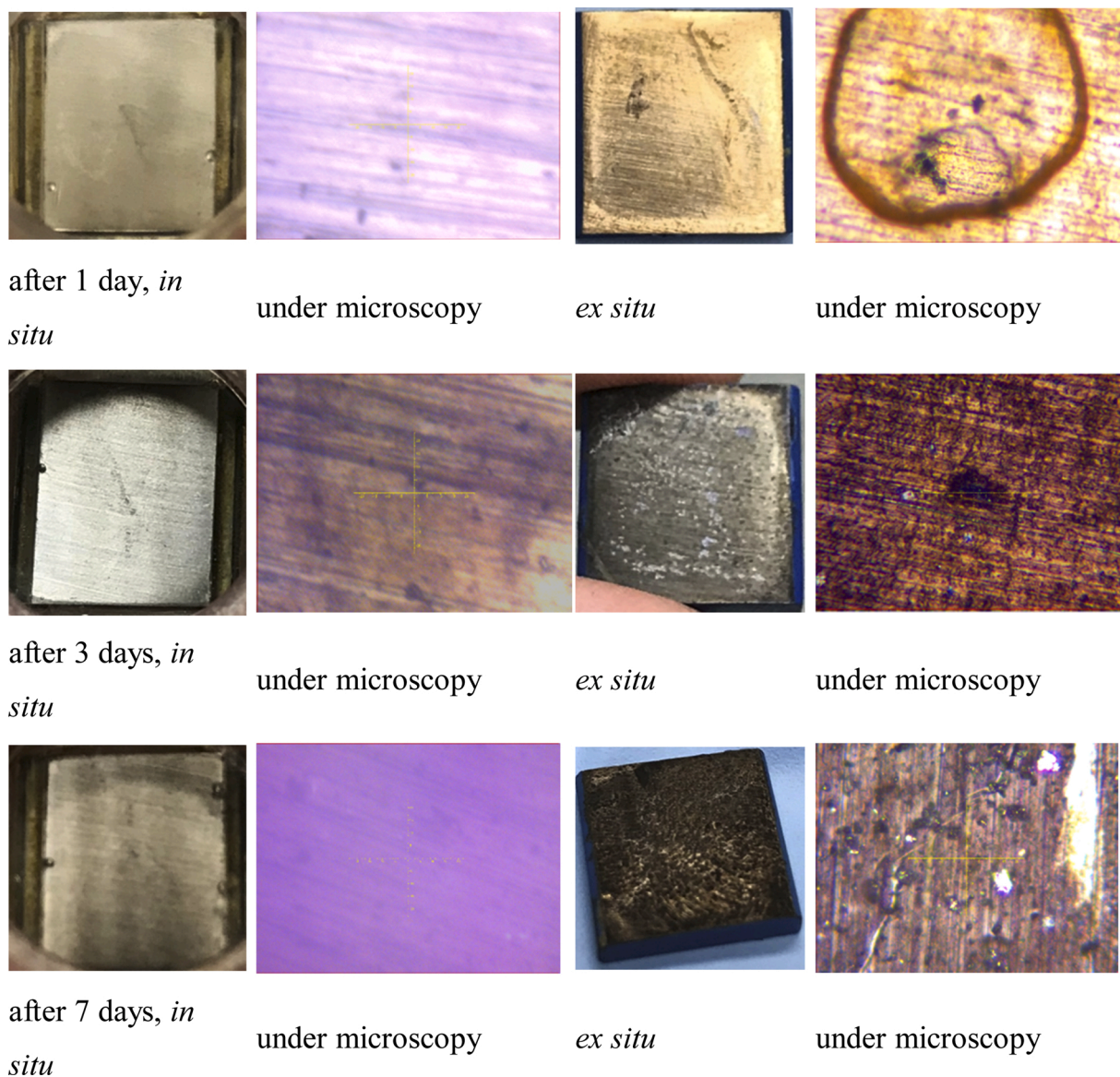


Fig. 22. Surface condition of the corroding X65 steel specimens under naked eye and microscopy after 1, 3 and 7 days exposure (the baseline condition at 30 °C, pH 5.01 ± 0.01, 0.97 bar CO<sub>2</sub>, 0.04 mbar H<sub>2</sub>S, 300 rpm stir bar, 7 days, [O<sub>2</sub>]<sub>(aq)</sub> = 5 ~ 7 ppb<sub>(w)</sub>).

cm<sup>-1</sup>) and torsion ( $\tau$ , 86 and 150–191 cm<sup>-1</sup>). However, the stretching mode related peak of S—S bond around 473 cm<sup>-1</sup> was missing, although it is usually a strong peak at 25 °C in S<sub>8</sub> crystals. A reported Raman application on chemisorption of H<sub>2</sub>S on copper impregnated activated carbon showed that the chemisorbed product was CuS [84]. Therefore, the S<sub>ads</sub>(Fe) Raman spectrum should feature the same peaks as mackinawite at around 208 ~ 218 cm<sup>-1</sup> (lattice vibration) and 281 ~ 298 cm<sup>-1</sup> (symmetric stretching). However, once again, the peaks around 282 cm<sup>-1</sup> are missing. Either the single broadened peak around 150 ~ 200 cm<sup>-1</sup> in the *in situ* Raman spectra potentially related to the bending or to the torsion of the Fe-S bond without showing much stretching activity. At least the *ex situ* Raman spectrum shows that this layer featured the two characteristic peaks of mackinawite after being retrieved from the aqueous solution. More work, such as surface enhancement, is needed to obtain more detailed structural information about the S<sub>ads</sub>(Fe).

### 3.7. Pitting on mild steel in marginally sour environments with oxygen ingress

This *in situ* Raman microscopy study was originated from the pitting mechanism study of mild steel in marginally sour environments [19]. As a result, it has been found that the protective layer in this type of pitting is the H<sub>2</sub>S chemisorption layer on the steel surface or the 2D precursor of mackinawite, denoted as S<sub>ads</sub>(Fe). Oxygen ingress, if there is any, could oxidize this protective layer in small spots. Depending on the surface pH, either the layer will be dissolved or transformed into Fe<sub>3</sub>O<sub>4</sub>, as depicted in Fig. 19. Steel surface would be exposed to the corrosive H<sub>2</sub>CO<sub>3</sub> aqueous solution during this process, that is how the pits initiated. This type of pitting is inherently distinct from the classic pitting mechanism of the passive system, which is evident by the fact that the anodic polarization curve of the mild steel in H<sub>2</sub>S/CO<sub>2</sub> environments shows no passive-transpassive behavior. Due to the common mistake of applying the classic pitting mechanism of the passive system on sour corrosion, the author of this work will publish such evidence in future publications.

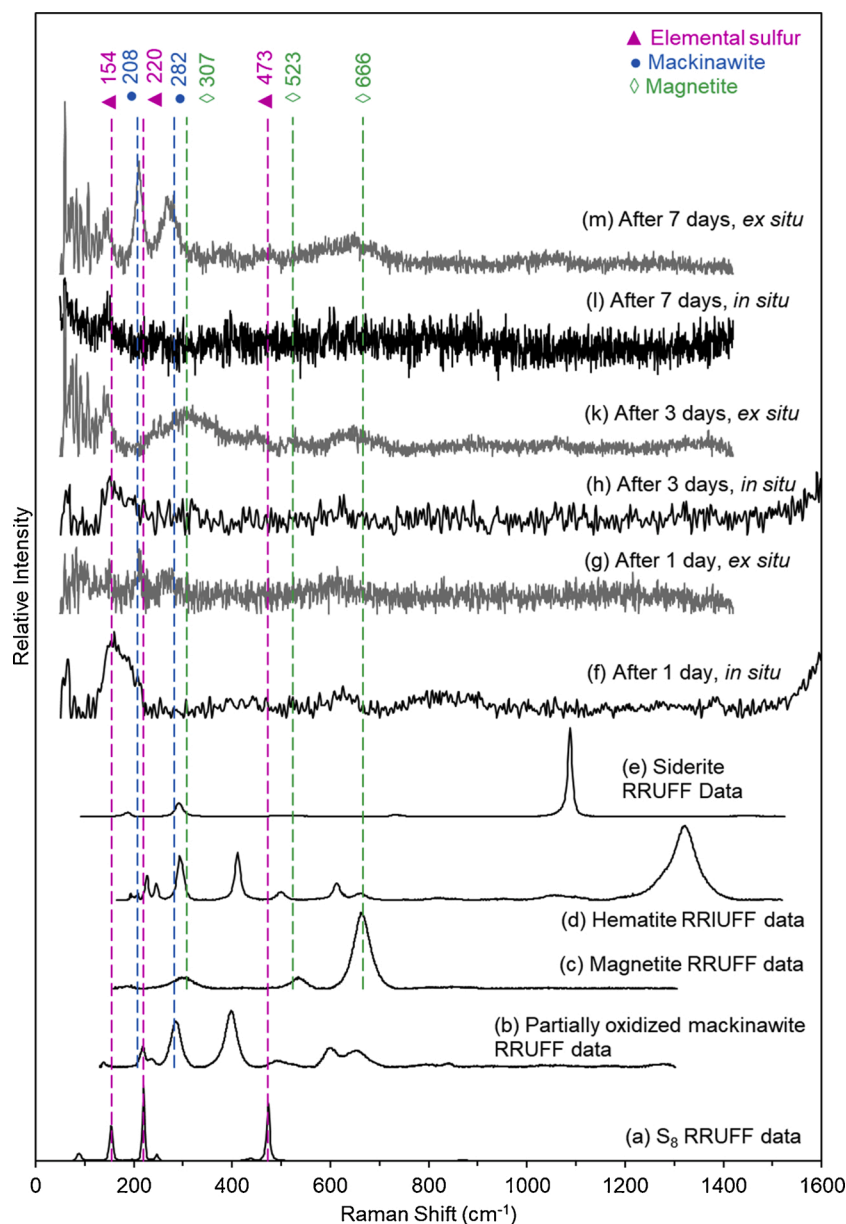


Fig. 23. *In situ* and *ex situ* Raman spectra of the corroding surface after 1, 3, 7 days of exposure. (30 °C, initial pH = 5.01,  $p\text{CO}_2 = 0.97$  bar,  $p\text{H}_2\text{S} = 40$  mbar,  $[\text{O}_2]_{\text{aq}} = 5\sim 7$  ppb<sub>(w)</sub>).

#### 4. Conclusions

Due to the high reactivity between dissolved oxygen and  $\text{H}_2\text{S}$ /iron sulfides, standard analytical tools that required *ex situ* analysis are often not ideal for the analysis of generated surface layers during sour corrosion. In contrast, *in situ* Raman constitutes a promising tool in terms of phase identification of the corrosion product layers formed in  $\text{H}_2\text{S}$  corrosion. This method was implemented, and the preliminary findings are outlined below:

- An *in situ* Raman flow cell was designed, fabricated in-house using 3D printing and implemented in an existing glass cell setup enabling the study of corrosion product layer formation and transformation during experiments.  $\text{O}_2$  ingress could be controlled to an acceptable level and a good seal of the cell could be maintained after being disconnected from the flow system to facilitate anaerobic Raman analysis;

- Aqueous sulfate species concentration lower than 0.01 mol/L cannot be detected by Raman spectroscopy using the experimental setup developed in this work;
- *Ex situ* Raman spectra showed that mackinawite layers were sensitive to oxidation in air, especially under the localized heating effect of the Raman laser;
- *In situ* Raman spectra showed that mackinawite layers were sensitive to partial oxidation in the aqueous solution by traces of dissolved oxygen ( $[\text{O}_2]_{\text{aq}} > 3$  ppb<sub>(w)</sub>);
- *In situ* Raman spectra could identify very thin layers (less than 300 nm thickness), be it amorphous or nanocrystalline mackinawite, through the glass lens and aqueous solution;
- *In situ* Raman spectra failed to identify the chemisorbed mackinawite layer –  $\text{S}_{\text{ads}}(\text{Fe})$ , while *ex situ* Raman spectra achieved it successfully.

#### Funding

This work was supported by the corrosion center joint industry

project; Institute for Corrosion and Multiphase Technology, Ohio University, 342 West State Street, Athens, OH, 45,701, USA.

### Author statement

Wei Zhang: Conceptualization, Methodology, Formal analysis, Investigation, Data Curation, Writing - Original Draft, Visualization

David Young: Conceptualization, Methodology, Writing - Review & Editing

Bruce Brown: Methodology, Resources, Writing - Review & Editing, Project administration

Cody Shafer: Methodology, Visualization

Fei Lu: Methodology, Writing - Review & Editing

Ezechukwu Anyanwu: Data Curation

Marc Singer: Conceptualization, Writing - Review & Editing, Supervision, Funding acquisition.

### Data availability statement

The raw/processed data required to reproduce these findings cannot be shared at this time due to technical or time limitations. They are available to readers upon email request to the Institute of Corrosion and Multiphase Technology.

### Declaration of Competing Interest

The authors declare that they have no known competing financial interests or personal relationships that could have appeared to influence the work reported in this paper.

### Acknowledgements

The author would like to thank Bruker scientist, Peng Wang for her technical support in application of Raman microscopy.

### References

- [1] H. Uhlig, Passivity in metals and alloys, *Corro. Sci.* 19 (1979) 777–791.
- [2] J.R. Galvele, Transport processes and the mechanism of pitting of metals, *J. Electrochem. Soc.* 123 (1976) 464.
- [3] G.S. Frankel, Pitting corrosion of metals: a review of the critical factors, *J. Electrochem. Soc.* 145 (6) (1998) 2186–2198.
- [4] R. Newman, Pitting corrosion of metals, *Electrochem. Soc. Interface* 19 (1) (2010) 33–38.
- [5] H. Strehblow, Mechanisms of pitting corrosion, in: P. Marcus (Ed.), *Corrosion Mechanisms in Theory and Practice*, Marcel Dekker, Inc, 2002.
- [6] A. Kahyarlian, M. Achour, S. Nesić, CO<sub>2</sub> corrosion of mild steel. Trends in Oil and Gas Corrosion Research and Technologies, Production and Transmission, Woodhead Publishing Series in Energy, 2017, pp. 149–190.
- [7] F. Fehlner, M. Graham, Thin oxide film formation on metals, in: P. Marcus (Ed.), *Corrosion Mechanisms in Theory and Practice*, Marcel Dekker, Inc, 2002.
- [8] B. MacDougall, M. Graham, Growth and stability of passive films, in: P. Marcus (Ed.), *Corrosion Mechanisms in Theory and Practice*, Marcel Dekker, Inc., 2002.
- [9] R. Revie, B. Baker, J. Bockris, The Passive film on iron: an application of Auger electron spectroscopy, *J. Electrochem. Soc.* 122 (1975) 1460.
- [10] M. Seo, J.B. Lumsden, R.W. Staehle, An AES analysis of oxide films on iron, *Surf. Sci.* 50 (2) (1975) 541–552.
- [11] A. Machet, A. Galtayries, S. Zanna, L. Klein, V. Maurice, P. Jolivet, M. Foucault, P. Combrade, P. Scott, P. Marcus, XPS and STM study of the growth and structure of passive films in high temperature water on a nickel-base alloy, *Electrochim. Acta* 49 (22–23) (2004) 3957–3964.
- [12] W.E. O'Grady, Mössbauer study of the passive oxide film on Iron, *J. Electrochem. Soc.* 127 (3) (1980) 555–563.
- [13] J. Han, S. Nesić, Y. Yang, B.N. Brown, Spontaneous passivation observations during scale formation on mild steel in CO<sub>2</sub> brines, *Electrochim. Acta* 56 (2011) 5396–5404.
- [14] S. Gao, B. Brown, D. Young, M. Singer, Formation of iron oxide and iron sulfide at high temperature and their effects on corrosion, *Corros. Sci.* 135 (2018) 167–176.
- [15] J. Ning, Y. Zheng, B. Brown, D. Young, S. Nesić, The role of iron sulfide polymorphism in localized H<sub>2</sub>S corrosion of mild steel, *Corros. J.* 73 (2016) 155–168.
- [16] L.G. Benning, R.T. Wilkin, H.L. Barnes, Reaction pathways in the Fe–S system below 100° C, *Chem. Geol.* 167 (2000) 25–51.
- [17] S. Navabzadeh Esmaeely, W. Zhang, B. Brown, M. Singer, S. Nesić, Localized corrosion of mild steel in marginally sour environments, *Corros. J.* 73 (9) (2017) 1098–1106.
- [18] W. Zhang, B. Brown, D. Young, Gheorghe Bota, S. Nesić, M. Singer, Pitting of mild steel in marginally sour environments – part I: a parametric study based on protective layers formation, *Corros. Sci.* 183 (2021), 109305.
- [19] W. Zhang, David Young, Bruce Brown, M. Singer, Pitting of mild steel in marginally sour environments – part II: pit initiation based on the oxidation of the chemisorbed FeS layers, *Corros. Sci.* 184 (2021), 109337.
- [20] W. Zhang, Initiation and Propagation of Localized Corrosion of Mild Steel in Marginally Sour Environments, *PhD Dissertation*, Ohio University, 2020.
- [21] D. Rickard, G.W. Luther III, Chemistry of iron sulfides, *Chem. Rev.* 107 (2007) 514–562.
- [22] S.N. Smith, E.J. Wright, Prediction of minimum H<sub>2</sub>S levels required for slightly sour corrosion. NACE Corrosion Conf., Paper no. 11, NACE International, Houston TX, 1994.
- [23] M.D. Fontana, K.B. Mabrouk, T.H. Kauffmann, Raman spectroscopic sensors for inorganic salts, *Spectrosc. Prop. Inorg. Organomet. Compd.* 44 (2013) 40–67.
- [24] K. Furic, I. Ciglencecki, B. Cosovic, Raman spectroscopic study of sodium chloride water solutions, *J. Mol. Struct.* 550–551 (2000) 225–234.
- [25] G. Genchev, A. Erbe, Raman spectroscopy of mackinawite FeS in anodic iron sulfide corrosion products, *J. Electrochem. Soc.* 163 (6) (2016) C333–C338.
- [26] J.-A. Bourdoiseau, M. Jeannin, R. Sabot, C. Rémazeilles, Ph. Refait, Characterisation of mackinawite by Raman spectroscopy: effects of crystallisation, drying and oxidation, *Corros. Sci.* 50 (2008) 3247–3255.
- [27] M.C. Di Bonaventura, Effect of Flow on the Formation of Iron Carbonate and Influence of Exposed Iron Carbide Layer, Master Thesis, Ohio University, Chemical Engineering, 2017.
- [28] M. Kalbac, H. Farhat, J. Kong, P. Janda, L. Kavan, M.S. Dresselhaus, Raman spectroscopy and in situ Raman spectroelectrochemistry of bilayer <sup>12</sup>C/<sup>13</sup>C graphene, *Nano Lett.* 11 (2011) 1957–1963.
- [29] W.T.E. van den Beld, M. Odijk, R.H.J. Vervuurt, J.-W. Weber, A.A. Bol, A. van den Berg, J.C.T. Eijke, In-situ Raman spectroscopy to elucidate the influence of adsorption in graphene electrochemistry, *Sci. Rep.* 7 (45080) (2017), <https://doi.org/10.1038/srep45080>.
- [30] By Thyphoon7979 - Own work, CC BY-SA 4.0, <https://commons.wikimedia.org/w/index.php?curid=59883279>.
- [31] A. Buckley, The surface oxidation of pyrite, *Appl. Surf. Sci.* 27 (1987) 437–452.
- [32] K. Furic, I. Ciglencecki, B. Cosovic, Raman spectroscopic study of sodium chloride water solutions, *J. Mol. Struct.* 550–551 (2000) 225–234.
- [33] A.R. Lennie, S.A.T. Redfern, P.E. Champness, C.P. Stoddart, P.F. Schofield, D. J. Vaughan, Transformation of mackinawite to greigite: an in-situ X-ray powder diffraction and transmission electron microscopy study, *Am. Mineral.* 82 (1997) 302–309.
- [34] R.A. Berner, Iron sulfides formed from aqueous solution at low temperatures and atmospheric pressures, *J. Geol.* 72 (1964) 293–306.
- [35] S. Boursiquot, M. Mullet, M. Abdelmoula, J.-M. Génin, J.-J. Ehrhardt, The dry oxidation of tetragonal FeS<sub>1-x</sub> mackinawite, *Phys. Chem. Miner.* 28 (2001) 600–611.
- [36] M. Mullet, S. Boursiquot, M. Abdelmoula, J.-M. Génin, J.-J. Ehrhardt, Surface chemistry and structural properties of mackinawite prepared by reaction of sulfide with metallic iron, *Geochim. Cosmochim. Acta* 66 (2002) 829–836.
- [37] A. Boughriet, R. Figueiredo, J. Laureyans, P. Recourt, Identification of newly generated iron phases in recent anoxic sediments: <sup>57</sup>Fe Mössbauer and micro Raman spectroscopic studies, *J. Chem. Soc. Faraday Trans.* 93 (1997) 3209–3215.
- [38] G. Genchev, K. Cox, T.H. Tran, A. Sarfraz, C. Bosch, M. Spiegel, A. Erbe, Metallic, oxygen-containing reaction products after polarization of iron in H<sub>2</sub>S saturated saline solutions, *Corros. Sci.* 98 (2015) 725–736.
- [39] B.W.A. Sherar, P.G. Keech, D.W. Shoesmith, The effect of sulfide on the aerobic corrosion of carbon steel in near - neutral pH saline solutions, *Corros. Sci.* 66 (2013) 256–262, <https://doi.org/10.1016/j.corsci.2012.09.027>.
- [40] E.B. Hansson, M.S. Odziemkowski, R.W. Gillham, Formation of poorly crystalline iron mono sulfides: surface redox reactions on high purity iron, spectro electrochemical studies, *Corros. Sci.* 48 (2006) 3767–3783.
- [41] R. Downs, The RRUFF Project: an Integrated Study of the Chemistry, Crystallography, Raman and Infrared Spectroscopy of Minerals, 2014. <http://www.rruff.info>.
- [42] B.W.A. Sherar, P.G. Keech, D.W. Shoesmith, The effect of sulfide on the aerobic corrosion of carbon steel in near - neutral pH saline solutions, *Corros. Sci.* 66 (2013) 256–262, <https://doi.org/10.1016/j.corsci.2012.09.027>.
- [43] R. Downs, The RRUFF Project: an Integrated Study of the Chemistry, Crystallography, Raman and Infrared Spectroscopy of Minerals, 2014. <http://www.rruff.info>.
- [44] R. Downs, The RRUFF Project: an Integrated Study of the Chemistry, Crystallography, Raman and Infrared Spectroscopy of Minerals, 2014. <http://www.rruff.info>.
- [45] R. Downs, The RRUFF Project: an Integrated Study of the Chemistry, Crystallography, Raman and Infrared Spectroscopy of Minerals, 2014. <http://www.rruff.info>.
- [46] D. Neff, P. Dillmann, L. Bellot-Gurlet, G. Beranger, Corrosion of iron archaeological artefacts in soil: characterisation of the corrosion system, *Corros. Sci.* 47 (2005) 515–535.
- [47] R. Downs, The RRUFF Project: an Integrated Study of the Chemistry, Crystallography, Raman and Infrared Spectroscopy of Minerals, 2014. <http://www.rruff.info>.

- [48] L. Bellot-Gurlet, D. Neff, S. Reguer, J. Monnier, M. Saheb, P. Dillmann, Raman studies of corrosion layers formed on archaeological irons in various media, *J. Nano Res.* 8 (2009) 147.
- [49] P. Colomban, S. Cherifi, G. Despert, Raman identification of corrosion products on automotive galvanized steel sheets, *J. Raman Spectrosc.* 39 (2008) 881.
- [50] M.K. Nieuwoudt, J.D. Comins, I. Cukrowski, The growth of the passive film on iron in 0.05 M NaOH studied in situ by Raman micro-spectroscopy and electrochemical polarisation. Part I: near-resonance enhancement of the Raman spectra of iron oxide and oxyhydroxide compounds, *J. Raman Spectrosc.* 42 (2011) 1335.
- [51] R. Downs, The RRUFF Project: an Integrated Study of the Chemistry, Crystallography, Raman and Infrared Spectroscopy of Minerals, 2014. <http://www.ruff.info>.
- [52] R. Downs, The RRUFF Project: an Integrated Study of the Chemistry, Crystallography, Raman and Infrared Spectroscopy of Minerals, 2014. <http://www.ruff.info>.
- [53] R. Downs, The RRUFF Project: an Integrated Study of the Chemistry, Crystallography, Raman and Infrared Spectroscopy of Minerals, 2014. <http://www.ruff.info>.
- [54] E. Paparazzo, XPS and auger spectroscopy studies on mixtures of the oxides SiO<sub>2</sub>, Al<sub>2</sub>O<sub>3</sub>, Fe<sub>2</sub>O<sub>3</sub> and Cr<sub>2</sub>O<sub>3</sub>, *J. Electron. Spectrosc. Relat. Phenom.* 43 (1987) 97.
- [55] P. Mills, J.L. Sullivan, A study of the core level electrons in iron and its three oxides by means of X-ray photoelectron spectroscopy, *J. Phys. D.* 16 (1983) 723.
- [56] B.J. Tan, K.J. Klabunde, P.M.A. Sherwood, X-ray photoelectron spectroscopy studies of solvated metal atom dispersed catalysts. Monometallic iron and bimetallic iron-cobalt particles on alumina, *Chem. Mater.* 2 (1990) 186.
- [57] J. Haber, J. Stoch, L. Ungier, X-ray photoelectron spectra of oxygen in oxides of Co, Ni, Fe and Zn, *J. Electron. Spectrosc. Relat. Phenom.* 9 (1976) 459.
- [58] Y.S. Lee, H.T. Kim, K.O. Yoo, Effect of ferric oxide on the high-temperature removal of hydrogen sulfide over ZnO-Fe<sub>2</sub>O<sub>3</sub> mixed metal oxide sorbent, *Ind. Eng. Chem. Res.* 34 (1995) 1181.
- [59] D. Brion, Etude par spectroscopie de photoelectrons de la degradation superficielle de FeS<sub>2</sub>, CuFeS<sub>2</sub>, ZnS et PbS a l'air et dans l'eau, *Appl. Surf. Sci.* 5 (1980) 133.
- [60] G.C. Allen, M.T. Curtis, A.J. Hooper, P.M. Tucker, X-Ray photoelectron spectroscopy of iron-oxygen systems, *J. Chem. Soc. Dalton Trans.* 14 (1974) 1525.
- [61] R.M. Torres Sanchez, E.M. Curt, C. Volzone, R.C. Mercader, A.L. Cavaliere, Study of Fe(II) oxidation in ground magnetite, *Mater. Res. Bull.* 25 (1990) 553.
- [62] P. Marcus, J.M. Grimal, The anodic dissolution and passivation of Ni-Cr-Fe alloys studied by ESCA, *Corros. Sci.* 33 (1992) 805.
- [63] N.S. McIntyre, D.G. Zetaruk, X-ray photoelectron spectroscopic studies of iron oxides, *Anal. Chem.* 49 (1977) 1521.
- [64] J.C. Carver, G.K. Schweitzer, T.A. Carlson, Use of X-ray photoelectron spectroscopy to study bonding in Cr, Mn, Fe, and Co compounds, *J. Chem. Phys.* 57 (1972) 973.
- [65] H. Binder, Investigations on the nature of the chemical bonds in iron-sulphur compounds using X-Ray photoelectron spectroscopy, *Z. Naturforsch. B28* (1973) 256.
- [66] R.V. Siriwardene, J.M. Cook, Interactions of SO<sub>2</sub> with sodium deposited on silica, *J. Colloid Interface Sci.* 108 (1985) 414.
- [67] X.R. Yu, F. Liu, Z.Y. Wang, Y. Chen, Auger parameters for sulfur-containing compounds using a mixed aluminum-silver excitation source, *J. Electron. Spectrosc. Relat. Phenom.* 50 (1990) 159.
- [68] A.R. Pratt, I.J. Muir, H.W. Nesbitt, X-ray photoelectron and Auger electron spectroscopic studies of pyrrhotite and mechanism of air oxidation, *Geochim. Cosmochim. Acta* 58 (1994) 827.
- [69] G. Panzner, B. Egert, The bonding state of sulfur segregated to  $\alpha$ -iron surfaces and on iron sulfide surfaces studied by XPS, AES and ELS, *Surf. Sci.* 144 (1984) 651.
- [70] M. Volmer-Uebing, M. Stratmann, A surface analytical and an electrochemical study of iron surfaces modified by thiols, *Appl. Surf. Sci.* 55 (1992) 19.
- [71] H. Peisert, T. Chasse, P. Streubel, A. Meisel, R. Szargan, Relaxation energies in XPS and XAES of solid sulfur compounds, *J. Electron. Spectrosc. Relat. Phenom.* 68 (1994) 321.
- [72] S. Chaturvedi, R. Katz, J. Guevremont, M.A.A. Schoonen, D.R. Strongin, XPS and LEED study of a single-crystal surface of pyrite, *Am. Mineral.* 81 (1996) 261.
- [73] Y.M. Shul'ga, V.I. Rubtsov, V.N. Vasilets, A.S. Lobach, N.G. Spitsyna, E. B. Yagubskii, EELS, XPS and IR study of C<sub>60</sub>-2S<sub>8</sub> compound, *Synth. Met.* 70 (1995) 1381.
- [74] B.J. Lindberg, K. Hamrin, G. Johansson, U. Gelius, A. Fahlmann, C. Nordling, K. Siegbahn, Molecular spectroscopy by means of ESCA II. Sulfur compounds. Correlation of electron binding energy with structure, *Phys. Scripta* 1 (1970) 286.
- [75] J.K. Heuer, J.F. Stubbins, An XPS characterization of FeCO<sub>3</sub> films from CO<sub>2</sub> corrosion, *Corros. Sci.* 41 (1999) 1231–1243.
- [76] I.N. Shabanova, V.A. Trapeznikov, A study of the electronic structure of Fe<sub>3</sub>C, Fe<sub>3</sub>Al and Fe<sub>3</sub>Si by x-ray photoelectron spectroscopy, *J. Electron. Spectrosc. Relat. Phenom.* 6 (1975) 297.
- [77] H. Goretzki, P.V. Rosenstiel, S. Mandziej, Small area MXPS- and TEM-measurements on temper-embrittled 12% Cr steel, *Fres. Z. Anal. Chem.* 333 (1989) 451.
- [78] XPS Interpretation of Carbon - XPS Simplified, XPS Reference Table of Elements, Thermo Scientific™ Advantage™ Data System for XPS, <https://xpsimplified.com/elements/carbon.php>.
- [79] G.H. Kelsall, I. Thompson, Redox chemistry of H<sub>2</sub>S oxidation in the British gas streford process, Part I: thermodynamics of sulphur-water systems at 298 K, *J. Appl. Electrochem.* 23 (1993) 279–286.
- [80] L.V. Gurvich, I.V. Veys, C.B. Alcock (Eds.), Thermodynamic Properties of Individual Substances, 4th ed., Hemisphere Publishing Corp., New York, 1989. Retrieved from Thermodynamic Properties as a Function of Temperature, Section 5: Thermochemistry, Electrochemistry, and Kinetics, CRC Handbook of Chemistry and Physics: 5-61–84.
- [81] M.W. Chase, et al., JANAF thermochemical tables, 3rd ed, *J. Phys. Chem. Ref. Data* 14 (Suppl. 1) (1985). Retrieved from Thermodynamic Properties as a Function of Temperature, Section 5: Thermochemistry, Electrochemistry, and Kinetics, CRC Handbook of Chemistry and Physics: 5-61–84.
- [82] P. Marcus, E. Protopopoff, Potential-pH diagrams for adsorbed species, application to sulfur adsorbed on iron in water at 25 °C and 300 °C, *J. Electrochem. Soc.* 137 (9) (1990) 2709–2712.
- [83] B.A. Trofimov, L.M. Sinegovskaya, N.K. Gusarova, Vibrations of the S–S bond in elemental sulfur and organic polysulfides: a structural guide, *J. Sulfur Chem.* 30 (5) (2009) 518–554.
- [84] V. Piergrosso, C. Fasolato, F. Capitani, G. Monteleone, P. Postorino, P. Gislon, Application of Raman spectroscopy in chemical investigation of impregnated activated carbon spent in hydrogen sulfide removal process, *Int. J. Environ. Sci. Technol.* 16 (2019) 1227–1238.